MWIR and Visible nBn Photodetectors and Their Monolithically-Integration for Two-Color Photodetector Applications

by

Zhaoyu He

A Dissertation Presented in Partial Fulfillment
of the Requirements for the Degree
Doctor of Philosophy

Approved November 2016 by the
Graduate Supervisory Committee:

Yong-Hang Zhang, Chair
Dragica Vasileska
Michael Goryll
Shane R. Johnson

ARIZONA STATE UNIVERSITY

December 2016

ABSTRACT

This work demonstrates novel nBn photodetectors including mid-wave infrared (MWIR) nBn photodetectors based on InAs/InAsSb type-II superlattices (T2SLs) with charge as the output signal, and visible nBn photodetectors based on CdTe with current output. Furthermore, visible/MWIR two-color photodetectors (2CPDs) are fabricated through monolithic integration of the CdTe nBn photodetector and an InSb photodiode.

The MWIR nBn photodetectors have a potential well for holes present in the barrier layer. At low voltages of < -0.2 V, which ensure low dark current $<10^{-5}$ A/cm^2 at 77 K, photogenerated holes are collected in this well with a storage lifetime of 40 s. This charge collection process is an in-device signal integration process that reduces the random noise significantly. Since the stored holes can be readout laterally as in charge-coupled devices, it is therefore possible to make charge-output nBn with much lower noise than conventional current-output nBn photodetectors.

The visible nBn photodetectors have a CdTe absorber layer and a ZnTe barrier layer with an aligned valence band edge. By using a novel ITO/undoped-CdTe top contact design, it has achieved a high specific detectivity of 3×10^{13} cm-Hz$^{1/2}$/W at room temperature. Particularly, this CdTe nBn photodetector grown on InSb substrates enables the monolithic integration of CdTe and InSb photodetectors, and provides a platform to study in-depth device physics of nBn photodetectors at room temperature.

Furthermore, the visible/MWIR 2CPD has been developed by the monolithic integration of the CdTe nBn and an InSb photodiode through an n-CdTe/p-InSb tunnel junction. At 77 K, the photoresponse of the 2CPD can be switched between a 1-5.5 µm MWIR band and a 350-780 nm visible band by illuminating the device with an external

light source or not, and applying with proper voltages. Under optimum conditions, the 2CPD has achieved a MWIR peak responsivity of 0.75 A/W with a band rejection ratio (BRR) of 52 dB, and a visible peak responsivity of 0.3 A/W with a BRR of 18 dB. This 2CPD has enabled future compact image sensors with high fill-factor and responsivity switchable between visible and MWIR colors.

This work is dedicated to my wife, Shizhi Li, my parents, Zhixin Zhu and Junfu He, and my uncle, Dr. Zhihong Zhu, for their love and support to me over the years.

ACKNOWLEDGMENTS

I would like to thank my advisor Dr. Yong-Hang Zhang, for his guidance and supervision over the past few years. My research work would be impossible without his deep understanding and rich experience of optoelectronic semiconductors and photodetectors. Also, I have benefited greatly from his research mentality, such as the more simple, the more beautiful, always think from the very fundamental physics point of view, devote sufficient time and effort to the design of experimental procedures or processing steps to optimize the efficiency, treat the experimental data skeptically and rigorously, but never stop thinking creatively and freely. Finally, his emphasis on hands-on experience, communication skills and leadership will be very helpful for my future career.

I would also like to thank the other members of my committee, Dr. Shane Johnson, Dr. Dragica Vasileska and Dr. Michael Goryll for their advice and interest in my research. I am thankful to all the current and previous colleagues in our group for their help and mentoring. They are Dr. Oray Orkun Cellek, Dr. Ha Sul Kim, Dr. Shi Liu, Zhi-Yuan Lin, Xin-Hao Zhao, Dr. Preston Webster, Dr. Xiao-Meng Shen, Jacob Becker, Calli Campbell, Maxwell Lassise, Yuan Zhao and Dr. Martyn Fisher. I also appreciate the kind wire-bonding help of Brian Schultz and Dragan Grubisic from Laser Components DG Inc.

Additionally, I would also like to acknowledge the financial support through ARO MURI grant W911NF-10-1-0524 and AFOSR Grant FA9550-10-1-0129. I also acknowledge the use of facilities in the Center for Solid State Electronics Research for the device processing at Arizona State University.

TABLE OF CONTENTS

Page

LIST OF TABLES viii

LIST OF FIGURES ix

I INTRODUCTION 1

1.1 Infrared Photodetection 1

1.2 Visible Photodetection 8

1.3 nBn Photodetectors 11

1.4 Monolithically Integrated Multicolor Photodetectors 14

1.4.1 Electrical Addressing 16

1.4.2 Optical Addressing 20

1.5 Photodetector Specifications 24

1.5.1 Blackbody Responsivity 24

1.5.2 Spectral Responsivity 24

1.5.3 External Quantum Efficiency 25

1.5.4 Noise 25

1.5.5 Detectivity 26

1.5.6 Specific Detectivity 26

II MWIR NBN PHOTODETECTORS USING INAS/INASSB TYPE-II SUPERLATTICE 27

2.1 Chapter II Introduction 27

2.2 MBE Growth and Device Processing 28

2.3 Device Characterization 30

Page

2.3.2 Characterization Methods ... 30

2.3.3 Dark Current ... 38

2.3.4 Responsivity and D* ... 41

2.3.5 Charge Storage ... 44

2.4 Chapter II Summary ... 49

III MONOLITHICALLY INTEGRATED VISIBLE/MWIR CDTE-NBN/INSB-PN TWO-COLOR PHOTODETECTORS ... 51

3.1 Chapter III Introduction ... 51

3.2 CdTe/InSb Tunnel Junction ... 52

3.3 Visible CdTe nBn Photodetector ... 53

3.3.1 Device Structure and MBE Growth ... 53

3.3.2 Top Contact Optimization ... 56

3.3.3 Dark Current and Responsivity vs. Voltage ... 58

3.3.4 Spectral Responsivity and D* ... 62

3.4 MWIR InSb PIN Photodetector ... 64

3.5 CdTe/InSb Visible/MWIR Two-Color Photodetector ... 66

3.5.1 One Optical Bias ... 67

3.5.2 MBE Growth and Device Processing ... 68

3.5.3 Electrical and Optical Addressing ... 70

3.5.4 Band Switching ... 71

3.5.5 Device Specifications ... 74

3.6 Chapter III Summary ... 75

Page

IV DEVICE PHYSICS OF NBN PHOTODETECTORS 77

4.1 Chapter IV Introduction 77

4.2 Origin of the Dark Current 80

4.2.1 Carrier Generation, Recombination and Transport 80

4.2.2 Hole Impedance and Electrical Addressing 83

4.3 Two-color Photodetection 89

4.4 Analytical Equations 89

4.5 Chapter IV Summary 92

V CONCLUSIONS 93

REFERENCES 95

LIST OF TABLES

Table Page

1. Division of Infrared Radiation [1]. 1

2. Comprehensive Comparisons of the Advantages CCD and CMOS Image Sensors 10

3. Comprehensive Comparisons between nBn Photodetectors and PIN Photodetectors 14

4. The Electrical and Optical Bias Conditions for Different Detecting Modes of the Two CdTe/InSb 2CPDs. 72

5. The Specifications of the CdTe-PN/InSb-PN and the CdTe-nBn/InSb-PN 2CPDs 75

6. The Artificial Material Parameters of nBn_TCL, nBn_AL and nBn Used in Silvaco 86

LIST OF FIGURES

Figure Page

1. Transmission of IR Photons through the Atmosphere over a 6000 ft Horizontal Path at Sea Level Containing 17 mm of Precipitate Water [1]. 2

2. Hybrid IR FPA with Independently Optimized Signal Detection and Readout: (a) Indium Bump Technique; (b) Loophole Technique [18]. 6

3. Band Edge Profile and Mini-Bands of InAs/InAsSb Type-II Superlattcies (T2SL) [15]. Due to the Type-II Band Alignment, It Is Possible for the T2SL to Achieve a Narrower Band Gap than that of the Constituent Bulk III-V Compound Semiconductors. 7

4. Compound Semiconductors with Different Bandgap Energies and Lattices Constants [16]. 8

5. FPA Structure of CCD and CMOS Image Sensors and Their Signal Reading Out Methods [20]. 9

6. The Band Edge Diagram of a Typical nBn Device Replotted from Reference [25] 13

7. Schematic Diagram of a Monolithically-Intergraded Multicolor Photodetector and How Each Sub-detector Absorbs Its Designated Waveband Only. 16

8. Voltage-Addressed MWIR/LWIR Two-Color Photodetector [41]. (a) the Layer Structure of the Device Using an External DC Voltage Source to Switch between the LWIR Mode and the MWIR Mode. (b) If a Positive Bias is Applied on the Top, the Top LWIR Diode is Reversed, and the Device Has

Figure Page

the LWIR Response. (c) If a Negative Bias is Applied on the Top, the Bottom MWIR Diode is Reversed, and the Device Has the MWIR Response. 17

9. Under a Positive Bias of $V_1 + V_2$, the Quiescent Points of the MWIR and the LWIR Diodes are at the Black Dot and the Red Dot Respectively. By Calculating the First Derivative of the Curves, It Is Found that the AC Resistance of the MWIR Diode is Much Smaller Than that of the LWIR Diode.. 18

10. Equivalent AC Circuit of the Voltage-Addressing Two-Color Photodetector. 19

11. Schematic of the Optically Addressed, Two-Terminal, Multicolor Photodetector. The Detector Structure Consists of Multiple Photodiodes with Different Cutoff Wavelengths Connected in Series with Tunnel Diodes between Adjacent Photodiodes. The LEDs Optically Bias the Inactive Photodiodes in the Detector to Enable Single Color Detection [40].. 21

12. Crossover Points of the Dashed DC-Current Line with the I-V Curves Are the Q-Points of the Sub-detectors. The AC Resistances (r1, r2, …, rn-1, rn) Are the Reciprocal of the First Derivative of the I-V Curves at the Q-Points....... 22

13. Equivalent AC Circuit of the Optically-Addressed Multicolor Photodetector. The AC Resistances Are at the Q-Points and the AC Current Sources Are the Modulated Photocurrents. The Top Contact is Grounded in the AC Because the Bias on the Top Contact Is DC 22

Figure Page

14. Cross Section Schematic of the MWIR InAs/InAsSb T2SL nBn Detector Samples Fabricated at ASU, with Different Doping Concentrations and Thicknesses of the Absorber Region 29

15. Block Diagram of the Setup to Measure Blackbody Responsivity................. 32

16. The Modulation Factors for Different Chopping Conditions Using a Circular Blackbody Aperture and a Chopper with Radial Teeth in Circular Motion [44]... 34

17. Block Diagram of the Setup Used to Measure the Detector Noise................. 37

18. Layer Structures of the MWIR nBn and PIN Photodetectors Based on InAs/InAsSb T2SLs, in Both of which the Absorbers Are Unintentionally Doped as n-type and Are around 2.5 μm Thick 39

19. Dark Current is Greatly Suppressed in the nBn Photodetector Compared to the PIN Photodetector Based on MWIR InAs/InAsSb T2SLs. 40

20. Dark I-V Curves and Cross Section Schematics of Shallowly Etched nBn vs Single Element nBn Detectors. 41

21. (a) Dark Current and Responsivity at the Wavelength of 3.39 μm as Functions of the Applied Bias at the Temperature of 77 K (b) Normalized Responsivity Spectrum at 77 K in the MWIR InAs/InAsSb Superlattice nBn Photodetectors. 42

22. Specific Detectivity Spectra at 77 K for 2.5 μm Thick Devices with Different Absorber Doping Concentrations. 43

Figure Page

23. A Schematic Bandedge Diagram of the Devices under a Negative Bias. The Carriers Are Generated by Either Optical or Thermal Excitation in the Absorber, or Electron Band-to-Band Tunneling from the Barrier Layer to the Absorber Layer. Due to the Type-II Bandedge Alignment, the Electrons and Holes Get Accumulated at the Top-Contact-Layer/Barrier-Layer Interface .. 45

24. The Capacitance is Enhanced by 0.39 pF Under Light, which Suggests the Collection of the Photogenerated Holes by the Barrier Layer, and After the Light is Turned Off, the Capacitance Decays Slowly with a Time Constant of 40 s at 16.5 K under −0.1 V. 47

25. Current Decay Characteristic of the InAs/InAsSb nBn Photodetector at 77.6 K, -0.25 V after Light is Turned Off 48

26. Device Structure of the n-CdTe/n-InSb and n-CdTe/p-InSb Tunnel Junction Samples.. 52

27. Dark I-V Curves of the Highly Conductive n-CdTe/n-InSb and n-CdTe/p-InSb Hetero Tunnel-Junctions at 77 K 53

28. (a) Device Layer Structure of the CdTe nBn with a 1 μm Thick CdTe Absorber and a 50 nm Thick ZnTe as the Barrier Layer. (b) Band Edge Alignment of the CdTe nBn Photodetector 55

29. (a) CdTe nBn with Heavily Doped Top Contact Layer and Indium Contact. (b) CdTe nBn with no Top Contact and ITO Grown on the Barrier Layer Directly. (c) CdTe nBn with the Top Contact Layer and ITO Top Contact 57

Figure Page

30. (a) I-V and Responsivity-Voltage Characteristics at the Wavelength of 633 nm at Room Temperature. (b) Arrhenius Plot of the Dark Current as a Function of Temperature at -0.5 V and 0.5 V. 59

31. The Schematic Band Diagram of the CdTe nBn Photodetector under a Negative Bias Applied to the Top Contact, and with the Bottom Contact Grounded. The Carrier Generation-Recombination and Transport Processes are Shown..... 61

32. The Spectral Responsivity and External Quantum Efficiency of the CdTe nBn Photodetector under an Electrical Bias of -0.1 V at Room Temperature. 63

33. A High Specific Detectivity of up to 4×1013 cm-Hz1/2/W at Room Temperature is Achieved for the CdTe nBn Photodetector. A Flat Detectivity Plateau Covers the Whole Visible Light Range 63

34. Layer Structure of the InSb PIN Photodetector 64

35. Spectral Responsivity and Eternal Quantum Efficiencies of the InSb PIN Photodetector under 0 Bias at 77 K 65

36. Dark I-V Curves of the InSb PIN Photodetector at 77 K Before and after the Ammounium-Sulfide Surface Treatment..... 66

37. (a) Layer Structure of the CdTe-PN/InSb-PN Two-Color Photodetector. (b) Layer Structure of the CdTe-nBn/InSb-PN Two-Color Photodetector.. 69

38. Responsivities of (a) the CdTe-PN/InSb-PN 2CPD and (b) the CdTe-nBn/InSb-PN 2CPD as a Function of the Applied Electrical Bias when the Optical Bias (OB) is ON or OFF at a Temperature of 77 K. The MWIR

Figure Page

and Visible Responsivities are Measured Using Light Sources at Wavelengths of 3.39 µm and 650 nm Respectively. 71

39. (a) The Responsivity of the CdTe-PN/InSb-PN 2CPD Can be Switched between the Visible Band and the MWIR Band by Changing the Optical Bias Only under a Zero Electrical Bias. (b)The CdTe-nBn/InSb-PN 2CPD Has Responsivity Bands of Visible, MWIR and Red-Blind Visible which are Switchable by Changing Both the Optical Bias and the Electrical Bias......... 72

40. Equivalence of the Boundary Conditions on Hole Dark Current in the Back-to-Back Diode Structure (above), and the nBn Structure (below). The Identical Boundary Conditions in both Cases Justify the Use of the Back-to-Back Photodiode Equations to Describe the nBn Detector [76]....... 79

41. Carrier Transport and G-R Processes in the nBn Structure 81

42. The Gauss Theorem Analysis of the Hole Current in the nBn Structure........ 83

43. (a) The Simulated Four Characteristic Profiles: Conduction and Valence Band Edges, Electron and Hole Quasi Fermi Levels of the nBn at -0.14 V, (b) the Four Characteristic Profiles of the Artificial nBn_TCL at -0.1 V (c) the Four Characteristic Profiles of the Artificial nBn_AL at -0.05 V, (d) The Dark I-V Curves of the nBn, the nBn_TCL and the nBn_AL. (-0.1) + (-0.05) ≈ - 0.14 V! Temperature: 150K. The Contacts Are Set to be Ohmic.......................... 87

I INTRODUCTION

1.1 Infrared Photodetection

Infrared photodetection has broad applications in night vision, remote sensing, chemical detection, medical imaging, industry monitoring, earth resource survey, and astronomy. Infrared radiation is defined as light radiation with wavelength from 780 nm red light, to 1 mm microwaves. The division of infrared radiation wavelength ranges is shown below in Table 1, and is based on the limits of spectral bands of commonly used IR detectors [1].

Table 1 Division of infrared radiation [1].

Region(abbreviation)	Wavelength Range (μm)	Commercial Detection Materials
Near infrared (NIR)	0.78-1	Si
Short wavelength IR (SWIR)	1-3	PbS, InGaAs
Mid wavelength IR (MWIR)	3-6	InSb, PbSe, PtSi, HgCdTe
Long wavelength IR (LWIR)	6-15	HgCdTe
Very long wavelength IR (VLWIR)	15-30	
Far infrared (FIR)	30-100	
Submillimeter (SubMM)	100-1000	

All objects emit infrared radiations due to the vibration of the constituent atoms. The higher the temperature is, the stronger the atom vibrations are, and therefore the higher the average photon energy emitted from the object. In theory for a blackbody, the

distribution of the power density (or photon number flux) per wavelength and per unit area is given by the Planck's law as shown in Equation (1) and (2).

$$W(\lambda,T)=\frac{2\pi hc^2}{\lambda^5}\left[\exp\left(\frac{hc}{\lambda kT}\right)-1\right]^{-1}, \quad \text{W cm}^{-2}\ \mu\text{m}^{-1} \tag{1}$$

$$\mathrm{P}(\lambda,T)=\frac{2\pi c}{\lambda^4}\left[\exp\left(\frac{hc}{\lambda kT}\right)-1\right]^{-1}, \quad \text{photons s}^{-1}\ \text{cm}^{-2}\ \mu\text{m}^{-1} \tag{2}$$

where λ is the wavelength, T is the temperature, h is Planck's constant, c is the velocity of light and k is Boltzmann's constant.

For remote sensing, two important spectral windows of MWIR (3-5 μm) and LWIR (8-14 μm), are most widely used due to the absorption of gas molecules in the atmosphere. Figure 1 is a plot of the transmission through 6000 ft of air as a function of wavelength [1].

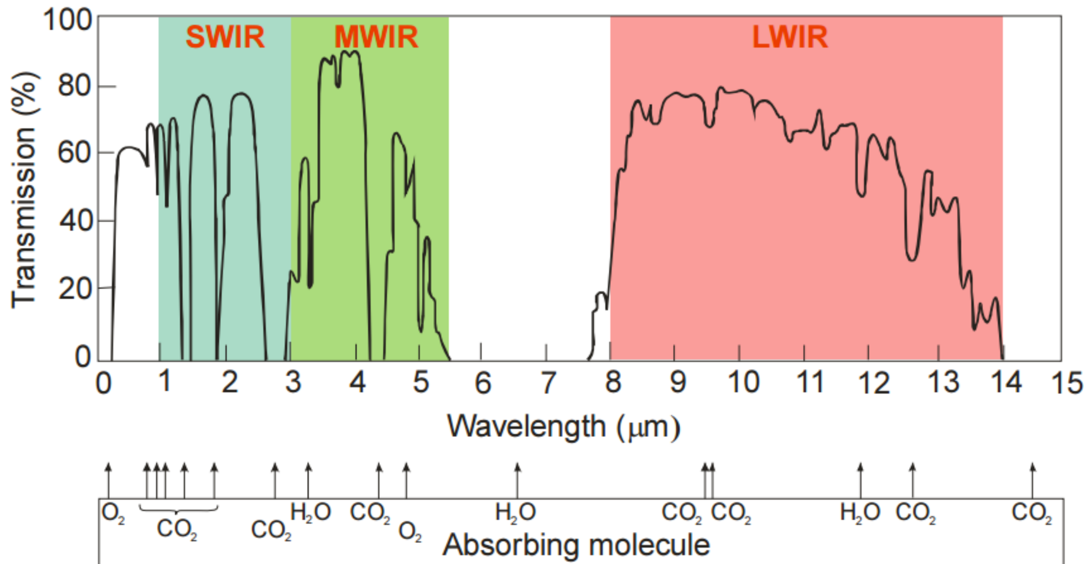

Figure 1 Transmission of IR photons through the atmosphere over a 6000 ft horizontal path at sea level containing 17 mm of precipitate water [1].

For an object at room temperature of 27 °C, the maximum power appears at the wavelength of 9.66 μm, and the maximum photon flux appears at 12.23 μm. Therefore, we need to use LWIR photodetectors with a cut-off wavelength longer than 13 μm to image room temperature objects such as humans, animals and plants without the aid of reflected light. Whereas MWIR photodetectors with a cut-off wavelength of 5.5 μm detect hot objects, with a temperature higher than 250 °C, such as engines and fires. The advantages of MWIR photodetectors and focal plane arrays (FPAs) over LWIR detectors include higher contrast, higher transmissivity in high humidity, higher working temperature (~200 K), and higher resolution due to smaller optical diffract [1]. By contrast, LWIR photodetectors and FPAs have better performance in fog, dust, winter haze conditions, higher immunity to atmospheric turbulence and reduced sensitivity to solar glints and fire flares [1].

Two kinds of infrared photodetectors are most widely used, semiconductor photodetectors and thermal detectors [1]. Semiconductor photodetectors usually have an absorber with direct band gap, so that light can efficiently excite an electron from the valence band to the conduction band and generate a free electron-hole pair. The photogenerated carriers are then collected by metal contacts under voltage biases. By contrast, in a thermal detector, the incident radiation is absorbed to change the temperature, and the temperature-induced change of physical properties, such as resistance generates an electrical output [1]. The semiconductor photodetectors usually have higher sensitivity and higher speed, and the author's study focuses on the semiconductor photodetectors.

It requires narrow-gap semiconductors with bandgap energies of smaller than 250 meV, such as HgCdTe, InGaAs, PbS and InSb to detect LWIR and MWIR light. Due to the narrow band gap, the intrinsic thermal G-R process in the materials can induce high dark current and noise, which can be generally suppressed by cooling down the photodetector. For MWIR photodetectors, a temperature of ~200 K using a thermoelectronic (TE) cooler ensures sufficiently low dark current, while for a LWIR photodetector, it is usually necessary to use liquid nitrogen to cool down the device to cryogenic temperatures near 77 K.

BLIP (background limited infrared photodetection) temperature is defined as a critical temperature at which the photodetector has a dark current equal to the photocurrent induced by the background radiation, given a field of view (FOV), and a background temperature [2]. As the temperature decreases, the dark current decreases, and at a certain threshold temperature point the noise of the dark current is equal to the noise induced by usually a 300 K surrounding environment with a 2π FOV. Below this threshold temperature, the dominate noise is caused by the 300 K environment radiation rather than the dark current, and cooling down the device temperature does not reduce the noise level in the device any more. This threshold temperature is called the BLIP temperature for 2π FOV and 300 K. Higher BLIP temperature is preferable because it means simpler and cheaper cryogenic system with lower power-consumption.

In order to achieve higher BLIP temperature for IR photodetectors while maintaining a high detectivity, the key is to suppress the dark current while keeping the quantum efficiency high. Generally, higher-quality material with long carrier lifetime is preferable because it ensures lower thermal generation dark current and a higher

possibility for the carriers to be collected before they recombine, or namely, higher quantum efficiency. Besides, other important material parameters such as absorption coefficient and carrier mobility are preferred to be high to ensure a high quantum efficiency. For instance, HgCdTe is the most well-studied and broadly-used infrared material with very long carrier lifetime of up to 10 μs, high absorption coefficient of ~ 5000 cm^{-1}, and high carrier mobility of 440 $cm^2V^{-1}s^{-1}$ [3][4].

Commercial infrared HgCdTe photodetectors include photoconductors (PC), photodiodes (PV), and avalanche photodiodes (APDs) [17]. Commercial infrared image sensors are comprised of 2D arrays of HgCdTe photodetectors connected with indium bumps to a Si read-out integrated circuits (ROIC) chip as a hybrid structure, which is often called a sensor chip assembly (SCA) as in Figure 2. These hybrid-packaged FPAs leverage the highly mature silicon IC fabrication technology, and have the advantage of near 100% fill factors [18]. High-resolution 2048×2048 MWIR and LWIR image sensors are commercially available.

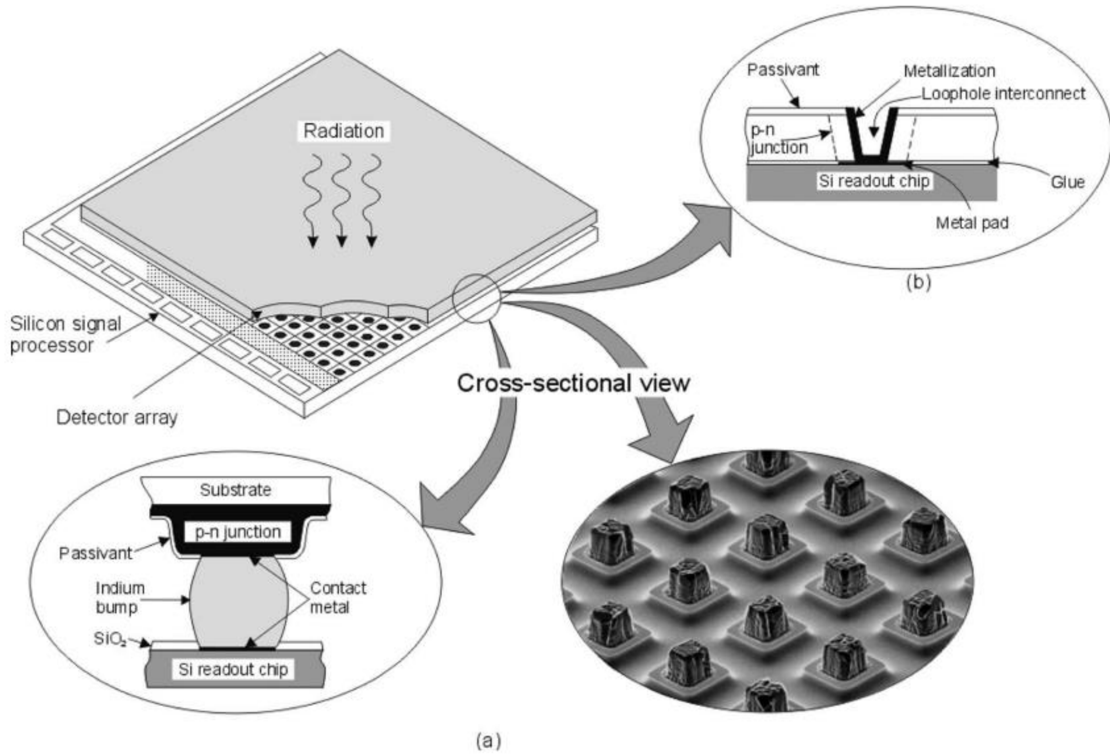

Figure 2 Hybrid IR FPA with independently optimized signal detection and readout: (a) indium bump technique; (b) loophole technique [18].

As a potential alternative to the commercial HgCdTe material, antimonide based T2SLs have attracted a lot of research interest. Antimonide based T2SLs are periodic thin-film structures consisting of two compound semiconductors with a type-II band gap alignment (Figure 3) and a 6.1 Å lattice constant, including GaSb, InAs, InSb and AlSb as in Figure 4. Due to the type-II band gap alignment, it is possible for the T2SL to achieve a narrower band gap than that of the constituent bulk III-V compound semiconductors. The band gap engineering of the T2SL is more flexible than for the HgCdTe because the band gap of the T2SL can be controlled by not only the alloy composition, but also the period thickness with a resolution down to one monolayer using

molecular beam epitaxy (MBE). Furthermore, the T2SL material has relatively lower manufacturing cost, better uniformity [5], suppressed Auger recombination and in theory, lower tunneling currents [6][7][8]. However, the most well studied LWIR InAs/(In)GaSb T2SLs have not yet reached the predicted high device performance [7]. One of the limiting factors is the low minority carrier lifetime of ~ 30 ns at 77 K [9][10]. Recently, it was reported that minority carrier lifetimes in LWIR InAs/InAsSb T2SLs are longer than 412 ns at 77 K [11], and in MWIR InAs/InAsSb T2SLs the lifetimes are up to 12.8 μs at 12 K [12]. These long carrier lifetimes are attributed to the suppression of SRH recombination rate due to the removal of Ga atoms [11]. Apart from long carrier lifetime, high absorption coefficient of 3500 cm^{-1} [13] and reasonable hole mobility of 60 $cm^2V^{-1}s^{-1}$ [14] are measured in MWIR InAs/InAsSb T2SLs with a 10 nm period. These high-quality materials suggest the potential to achieve an IR photodetector with high device performance.

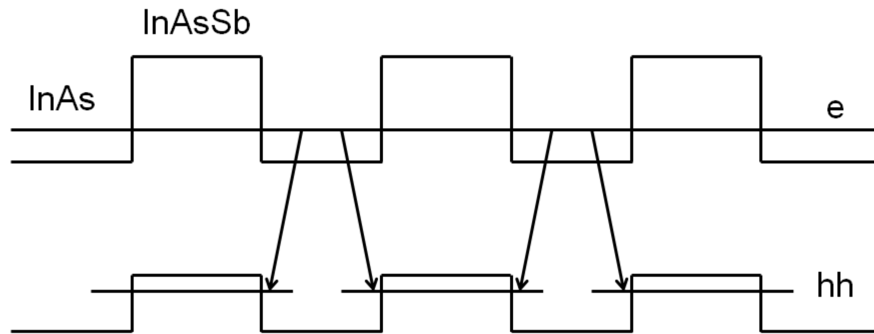

Figure 3 Band edge profile and mini-bands of InAs/InAsSb type-II superlattcies (T2SL) [15]. Due to the type-II band alignment, it is possible for the T2SL to achieve a narrower band gap than that of the constituent bulk III-V compound semiconductors.

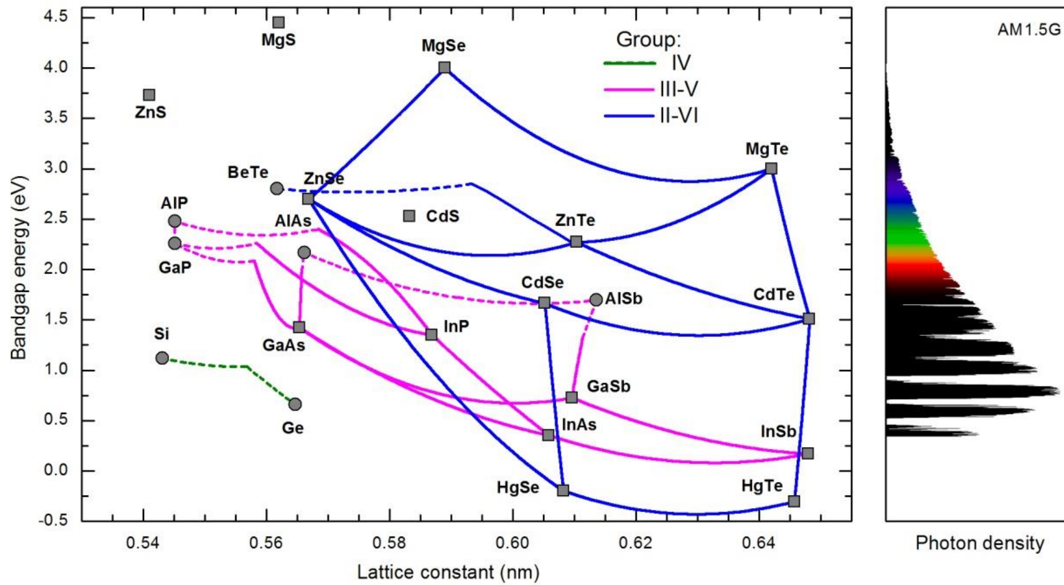

Figure 4 Compound semiconductors with different bandgap energies and lattices constants [16].

1.2 Visible Photodetection

The technology of visible photodetection is widely used in daily life, such as video imaging, optical communications, biomedical imaging, security monitoring, and motion detection [19]. Solid-state visible light photodetectors use semiconductors with much larger band gap (> 1 eV) than infrared semiconductors, and have the advantage of room-temperature operability. The most commonly used semiconductors for visible light photodetection include Si, GaAs, Ge, InGaAs, and AlGaAs. The most popular material Si has the advantages of low-cost, compatibility to the large-scale CMOS production and integration technologies. Whereas another popular yet more expensive material GaAs has

better optical properties due to its direct band gap and high speed due to its large electron mobility.

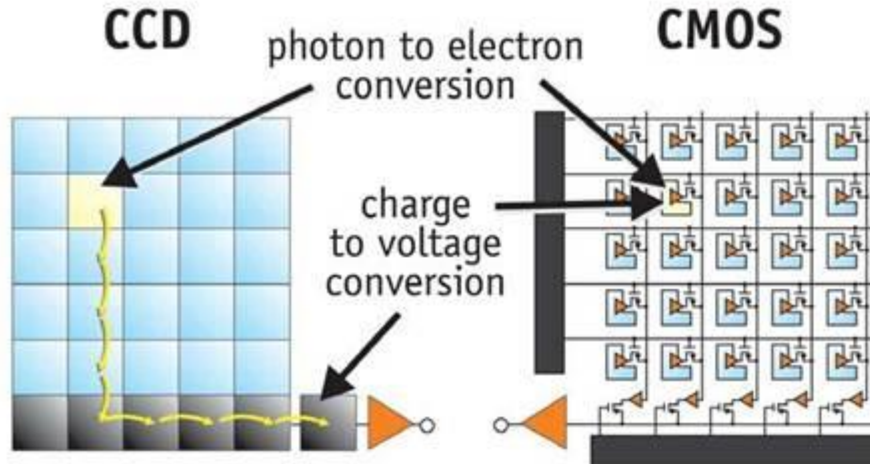

Figure 5 FPA structure of CCD and CMOS image sensors and their signal reading out methods [20].

The applications of visible photodetection have two realms, image sensing and optical communication. Leveraging the very large-scale integrated circuit (VLSIC) technologies, high-resolution silicon-based image sensors with large-scale photodetectors in a FPA have become highly mature, including CMOS and CCD image sensors as seen in Figure 5. In each pixel of the CMOS FPA, there are several functional transistors besides the photodiode, such as source-follower, selection, reset, transfer transistors [21]. As a result, CMOS have a lower fill-factor and higher fixed pattern noise than CCDs. This is because in a CCD, every pixel is nearly 100% filled with a photoactive metal-insulator-semiconductor structure. However, in the last decades, due to noise

suppression techniques, such as floating diffusion gate and correlated double sampling (CDS) circuits, CMOS image sensors have become increasingly competitive with CCD image sensors [21]. Even though CMOS still possesses higher noise than CCD, it has many dominant advantages over CCD, including lower cost due to its compatibility with the standard CMOS processing technology, lower power consumption, higher speed and random access [22]. Table 2 is a summary of the main advantages of CMOS and CCD image sensors [22].

Table 2 Comprehensive comparisons of the advantages CCD and CMOS image sensors

	Noise	Power Usage	Pixel Size	Dark Current	Fill Factor	Compatibility to CMOS Fabrication	Cost	Ransom Access
CCD	Low	High	Small	Low	High	No	High	No
CMOS	High	Low	Large	High	Low	Yes	Low	Yes

In the optical communication realm, non-imaging photodetectors or photoreceivers are widely used in analog RF and optical fiber communications. Strictly speaking, photodetectors for optical communication have photoresponse in the NIR wavelength range, such as 850 nm, 1310 nm and 1550 nm. However, such NIR photodetectors have similar bandgaps and properties to visible photodetectors, for instance bandgap greater than 1 eV and room temperature operation. Therefore, NIR photodetectors for optical communication are discussed in this chapter. High-speed

photodetectors with cutoffs up to tens of GHz are commercially available using materials with high mobility, such as GaAs, InGaAs and InP. To further increase the speed of the current optical communications techniques, silicon photonics on a chip have developed rapidly in the past decade due to its compatibility with mature silicon fabrication technologies. Novel Si or Si/Ge based optoelectronic devices are integrated onto silicon substrates, such as light emitting devices, modulators, photodetectors, and waveguides. Optical communication using these on-chip devices has the advantages of ultra-high speed and ultra-low power consumption, and the potential to achieve large-scale integration. In 2008, Yimin Kang et al. from Intel Corporation reported monolithic Ge/Si avalanche photodiodes with 340 GHz gain-bandwidth [23]. This is a significant progress that proves the gain-bandwidth product of a silicon avalanche photodiode can be higher than the mature, commercially available III-V compound avalanche photodetectors, especially InP photodetectors [23]. This work paves the way for the future development of low-cost, CMOS-based Ge/Si avalanche photodetectors operating at data rates of 40 Gb/s or higher [23].

1.3 nBn Photodetectors

An ideal photodetector possesses high quantum efficiency, low dark current, low noise, high dynamic range, large internal gain and high speed. Typical photodetector structures include photoconductors, pn or pin photodiodes, avalanche photodiodes, phototransistors and so on. For infrared photodetectors, suppressing the dark current is a major concern because of the narrow band gap of the absorber material. An infrared photoconductor can have high drift dark current due to the unintentional doping

concentration that is common for narrow-gap material. To suppress the drift current, a PIN structure is commonly used for infrared photodetectors because the depletion region has very low carrier concentration. However, due to the narrow band gap, infrared PIN photodetectors may suffer from the G-R dark current and band-to-band tunneling current in the depletion region under high voltage bias.

To further suppress the dark current, recently, a novel device structure—nBn, was proposed [24][25] as shown in Figure 6 [25]. It can be considered as an n-type photoconductor with a heterostructure barrier layer that has a conduction band barrier to block the electrons, while a valance band edge aligned to the absorber layer to let the holes pass freely. By doping the barrier layer lightly as n-type, it is possible to confine the voltage-induced depletion region of this device in the large-gap barrier layer and exclude it from the narrow-gap absorber layer [26]. As a result, not only the G-R dark current [26], but also the band-to-band tunneling current of the absorber layer can be greatly suppressed. In addition, for commonly used infrared materials such as InSb and InAsSb, there is a surface electron conduction-channel in the conduction band due to surface Fermi level pinning [27]. The barrier layer in the nBn structure can cut off the electron conduction channel on the surface [25] and suppress the surface leakage current significantly.

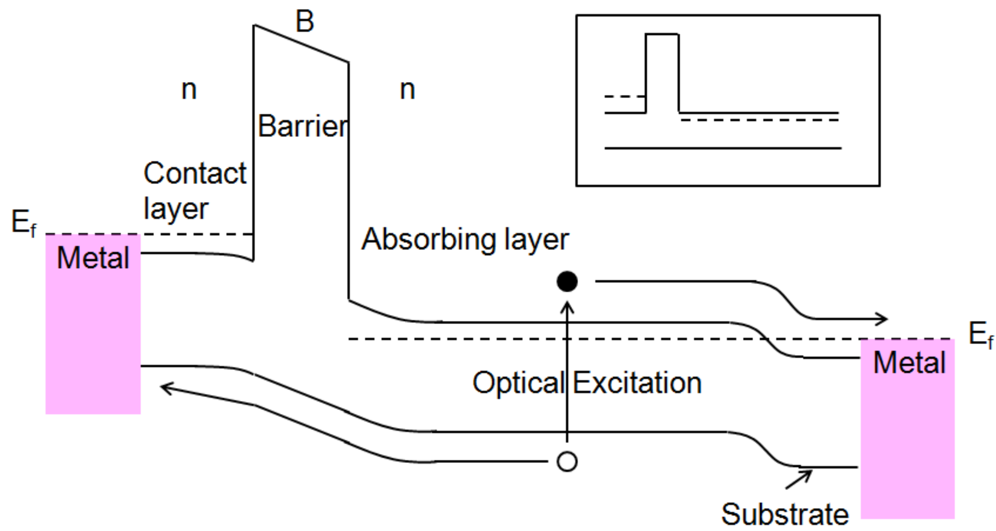

Figure 6 The band edge diagram of a typical nBn device replotted from Reference [25]

Infrared nBn photodetectors have been demonstrated using various material systems, such as InAsSb/AlAsSb [26][28], $Hg_xCd_{1-x}Te/Hg_yCd_{1-y}Te$ [29], (InAs/GaSb superlattice) / (InAs/AlSb superlattice) [30], and (InAs/InAsSb superlattice) / (InAs/AlSb superlattice) [31][32], where the left of the slash is the absorber material and the right of the slash is the barrier material. Comprehensive comparisons between typical nBn photodetectors and PIN photodetectors are listed in Table 3. Except diffusion dark current, major dark currents are suppressed in the nBn photodetector, such as G-R dark current, band-to-band tunneling current, and surface leakage current. Furthermore, due to the introduction of heterostructure layers, it is possible to realize two-color or even triple-color photodetection using the nBn structure. In addition, the bandwidth of the nBn photodetectors is close to that of PIN photodtectors because the response speed in both of these device structures is limited by the carrier lifetime.

Table 3 Comprehensive comparisons between nBn photodetectors and PIN photodetectors

	nBn photodetectors	PIN photodetectors
Diffusion Current (Quasi-neutral Region)	Same	Same
G-R Current (Depletion Region)	Lower	Higher
Band-to-band Tunneling Current	Lower	Higher
Surface Leakage Current	Lower	Higher
Possible Detection Colors	Two	One
Response Time	Same	Same

1.4 Monolithically Integrated Multicolor Photodetectors

Multicolor photodetectors (MCPDs) and focal plane arrays (FPA) are desirable for a variety of applications in defense, imaging, environmental monitoring, communications, and spectroscopy [33][34][35]. Typical monolithically-integrated MCPDs consist of multiple lattice-matched sub-detectors connected in series through tunnel junctions so that each sub-detector absorbs a specific band of the light, while allowing light with wavelength longer than its cutoff to pass to lower sub-detectors. The monolithic integration ensures a near 100% fill factor for the FPA and compatibility with single-color read-out circuit technologies. Compared to the conventional multicolor photodetection techniques that contain RGB color filter arrays or light splitting prisms, the major advantages of monolithically integrated MCPD include the highest possible fill factor, and absence of crude optical components. Traditional monolithically-integrated

two-color photodetectors (2CPDs) are comprised of either two back-to-back PN junctions [36][37], or nBn photodetectors with two absorber layers [38]. The output photocurrent of these 2CPDs is dominantly contributed by different junctions or absorber layers by using different voltage polarities, which is referred to as electrical addressing [36][37][38]. However, electrical addressing is challenging for monolithically-integrated MCPDs with more than two colors. Optical addressing is an alternative way to switch the colors of monolithically-integrated MCPDs by using external optical bias(es) to saturate the unwanted sub-detectors, thereby leaving the desired sub-detector as the only one active [39][40].

The general designing rules for the monolithic multicolor photodetector are discussed as follows. First, it is necessary to place the larger-gap sub-detectors on top of the narrower-gap ones as in Figure 7. In this way, each sub-detector absorbs a designated band of wavelength and lets the light with a wavelength longer than its cut-off be absorbed by the below sub-detectors. Second, the absorber thickness of each sub-detector should be at least longer than the optical penetration depth of its designated waveband, so that spectral crosstalk among the sub-detectors is minimized. Third, the materials at the interface between two adjacent sub-detectors should be heavily doped to achieve a tunnel junction, which can ensure a negligible voltage drop across the interface. Last, all the sub-detectors preferably need to be lattice-matched, so that the dislocation density is minimized and therefore it is easier to realize a high device performance.

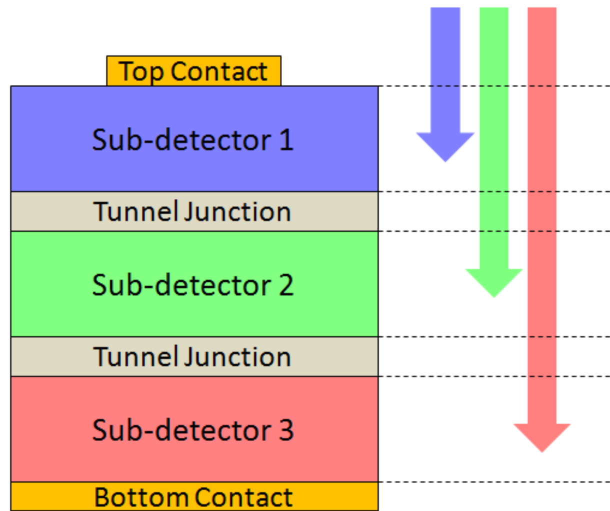

Figure 7 Schematic diagram of a monolithically-intergraded multicolor photodetector and how each sub-detector absorbs its designated waveband only.

In principle, a MCPD has photo response over the entire wavelength range that all the sub-detectors overlap. In practice however, we need to make only one of the sub-detectors active and the other ones inactive, so that the light intensity of only one specific waveband is read out, and spectral information of the incident light is extracted. This is referred to as addressing for multicolor photodetector. The conventional electrical addressing method and a recently proposed optical addressing method are discussed in the following two chapters.

1.4.1 Electrical Addressing

Conventionally, one practical way to realize the addressing of MCPDs is to use electrical DC voltage (bias). E. F. Schulte proposed a back-to-back double diodes structure [41] to achieve voltage-addressing two-color photodetector as in Figure 8. In

this structure, the active diode can be selected by applying a DC voltage in different polarities. For instance, as in Figure 8(b), if the DC voltage applied on the top contact is positive, the top LWIR diode is reversed and the bottom MWIR diode is forwarded. As a result, the top LWIR diode limits the current and the device has the LWIR response only, and *vice versa* if a negative DC voltage is applied as in Figure 8(c).

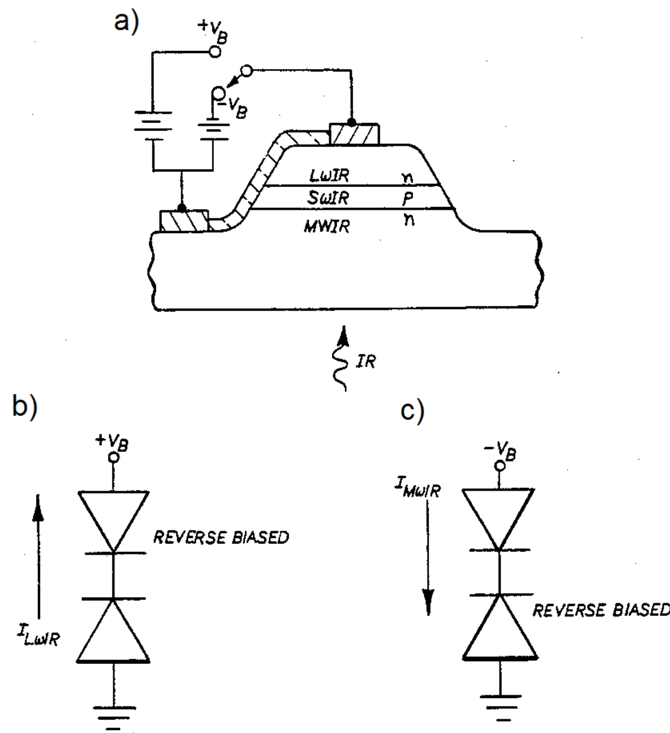

Figure 8 Voltage-addressed MWIR/LWIR two-color photodetector [41]. (a) the layer structure of the device using an external DC voltage source to switch between the LWIR mode and the MWIR mode. (b) If a positive bias is applied on the top, the top LWIR diode is reversed, and the device has the LWIR response. (c) If a negative bias is applied on the top, the bottom MWIR diode is reversed, and the device has the MWIR response.

The voltage-addressing behavior is explained comprehensively as in Figure 9. As the I-V curves of the sub-detectors shown in Figure 9, under a positive bias of $V_1 + V_2$, the quiescent points (Q-point) of the MWIR and the LWIR diodes are labeled by the black dot and the red dot respectively. By calculating the first derivatives of the I-V curves at the Q-points, it is found that the small-signal AC resistance of the MWIR diode is much smaller than that of the LWIR diode.

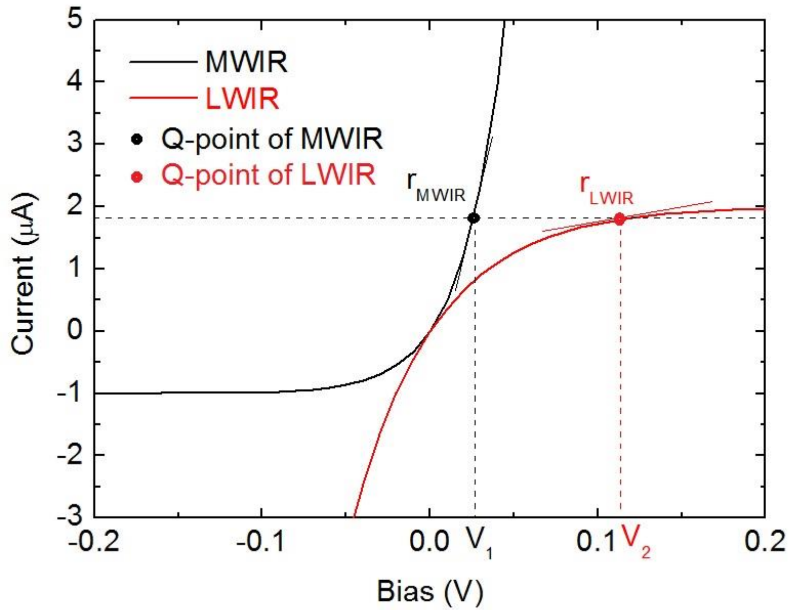

Figure 9 Under a positive bias of $V_1 + V_2$, the quiescent points of the MWIR and the LWIR diodes are at the black dot and the red dot respectively. By calculating the first derivative of the curves, it is found that the AC resistance of the MWIR diode is much smaller than that of the LWIR diode.

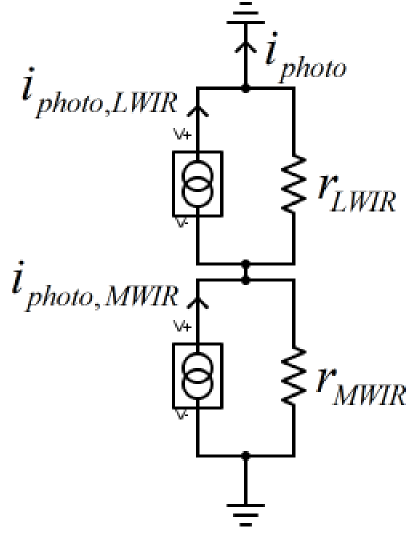

Figure 10 Equivalent AC circuit of the voltage-addressing two-color photodetector.

The equivalent AC circuit of the device is as in Figure 10, and the output photocurrent signal of the two-color photodetector is calculated as Equation (3).

$$i_{photo} = \frac{r_{LWIR}}{r_{LWIR} + r_{MWIR}} i_{photo,LWIR} + \frac{r_{MWIR}}{r_{LWIR} + r_{MWIR}} i_{photo,MWIR} \tag{3}$$

where i_{photo} is the output photocurrent, r_{MWIR} and r_{LWIR} are the AC resistances of the MWIR and the LWIR diodes respectively, $i_{photo,MWIR}$ and $i_{photo,LWIR}$ are the photocurrent of the MWIR and the LWIR diodes respectively. As discussed in the previous paragraph, under positive bias, because $r_{MWIR} << r_{LWIR}$, $i_{photo} \approx i_{photo,LWIR}$. Therefore, under the positive bias, the output photocurrent is approximately equal to the photocurrent generated by the LWIR diode. For the same reason, under the negative bias, the output photocurrent equals the photocurrent generated by the MWIR diode, approximately.

1.4.2 Optical Addressing

It is challenging to realize electrical addressing for MCPDs with more than two colors. An alternative method to realize the addressing for MCPDs is a recently proposed optical-addressing method [39][40]. Using this method, it is possible to realize the addressing for MCPDs with more than two colors, however, extra DC light sources are needed, such as LEDs and lasers to use this method. Figure 11 illustrates the operating principle of optically-addressed two-terminal multicolor photodetectors. Similar to Figure 7, the photodetector, as shown in Figure 11, consists of multiple photodiodes with different cutoff wavelengths, monolithically connected in series with tunnel diodes between adjacent photodiodes, with greater bandgap on the top and narrower bandgap at the bottom. Due to the series connection, the photodiode with the smallest current dictates the output of the device [40]. To optically-address this MCPD, all the sub-detectors except the desired one, are saturated by illuminating the device using DC light sources, which is referred to as optical biases, with wavelengths in the detection waveband of the undesired sub-detectors [40]. As a result, the desired sub-detector has an AC resistance much greater than all the other sub-detectors do, and the output AC photocurrent is contributed dominantly by this desired sub-detector.

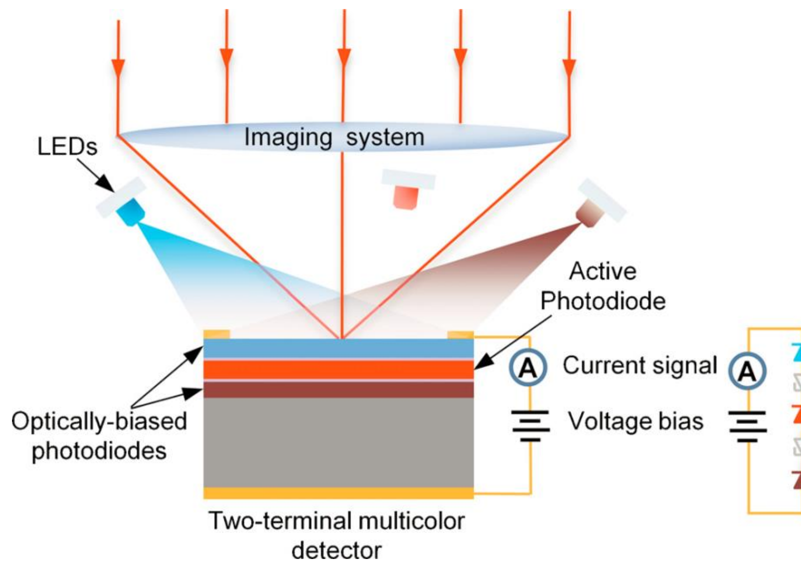

Figure 11 Schematic of the optically addressed, two-terminal, multicolor photodetector. The detector structure consists of multiple photodiodes with different cutoff wavelengths connected in series with tunnel diodes between adjacent photodiodes. The LEDs optically bias the inactive photodiodes in the detector to enable single color detection [40].

Figure 12 explains this optical-addressing behavior by analyzing the Q-points and the small-signal AC resistances of the sub-detector under a certain optical bias condition. For instance, if Sub-detector 2 is the desired sub-detector, all the sub-detectors except Sub-detector 2 should be optically biased. As a result, all the sub-detectors have very high reverse saturation current, except Sub-detector 2 which has negligible reverse saturation current due to thermal generation or the ambient radiation. Sub-detector 2 dictates the current through the MCPD and the dashed line in Figure 12 is the current line. The crossover points of the dashed current line with the I-V curves are the Q-points of the sub-detectors. The reciprocal of the first derivative of the I-V curve at the Q-point is the

AC resistance of each sub-detector. It can be found that Sub-detector 2 has an AC resistance much greater than those of all the other sub-detectors.

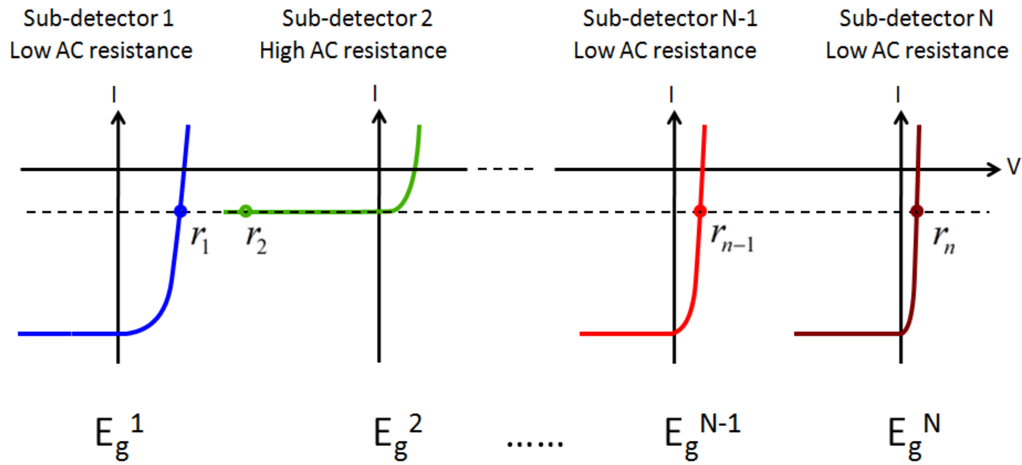

Figure 12 Crossover points of the dashed DC-current line with the I-V curves are the Q-points of the sub-detectors. The AC resistances (r_1, r_2, …, r_{n-1}, r_n) are the reciprocal of the first derivative of the I-V curves at the Q-points.

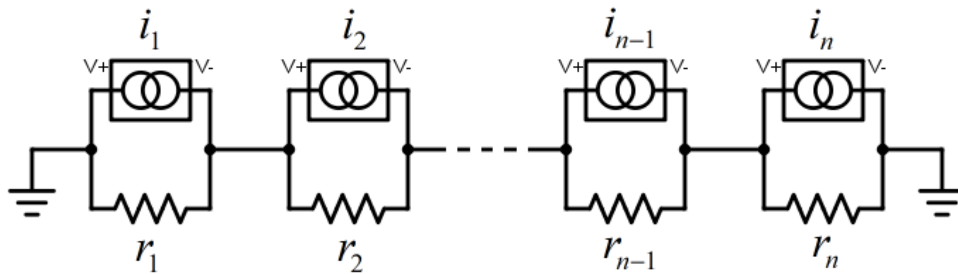

Figure 13 Equivalent AC circuit of the optically-addressed multicolor photodetector. The AC resistances are at the Q-points and the AC current sources are the modulated photocurrents. The top contact is grounded in the AC because the bias on the top contact is DC.

Using the equivalent AC circuit in Figure 13, the output photocurrent of the multicolor photodetector can be calculated as:

$$i_{output} = \sum_{k=1}^{n} \frac{i_k r_k}{\sum_{k=1}^{n} r_k} \approx i_2 \left(r_2 \gg r_{k \neq 2} \right) \tag{4}$$

where r_k is the AC resistance of Sub-detector k at the Q-point, i_k is the photocurrent of Sub-detector k ($k = 1, 2, ..., n-1, n$), which is in the same order of magnitude for every value of k. As in Equation (4), the output photocurrent is equal to the photocurrent of Sub-detector 2, which as an AC resistance much greater than that of every other sub-detector at the Q-point.

In short, to realize optical-addressing, we use optical bias, rather than the electrical bias as discussed in Chapter 1.5.1, to change the Q-points of the sub-detectors, and thus to change the AC resistance of the sub-detectors. As long as the desired sub-detector has an AC resistance much greater than that of the rest of the sub-detectors, the multicolor photodetector has the photo response from the desired sub-detector only.

Therefore, the key of addressing is to change the Q-points and hence the AC resistances of the sub-detectors. In this sense, the concept of optical-addressing and voltage-addressing can be unified. The only difference between them is that one uses a DC optical bias, and the other uses a DC electrical bias to change the Q-points of the sub-detectors. The voltage-addressing changes the DC voltage polarity on the device to change the Q-points, while the optical-addressing modifies the I-V curves of the sub-detectors to change the Q-points. In a future two-terminal multicolor photodetector, to realize more sophisticated addressing, the voltage-addressing and the optical-addressing can be used simultaneously.

1.5 Photodetector Specifications

To evaluate the quality of a photodetector, common specifications include dark current, cutoff wavelength, (spectral) responsivity, and (spectral) specific detectivity. The dark current means the current of a photodetector under no incident light at a certain voltage, and the cutoff wavelength is the longest detectable wavelength that is usually determined by the bandgap of the semiconductor. The definition of the (spectral) responsivity and (spectral) specific detectivity will be discussed comprehensively in this chapter.

1.5.1 Blackbody Responsivity

Blackbody Responsivity is the output photocurrent of a photodetector divided by the incident light power of a standard blackbody that typically has a temperature from 500 °C to 1100 °C.

$$R = \frac{I}{P} \tag{5}$$

where I is output current of the detector, and P is the total incident power on the device active area from the standard blackbody. The responsivity R has a unit of A/W.

1.5.2 Spectral Responsivity

Spectral responsivity is the responsivity as a function of the wavelength, which means the output photocurrent divided by the light power at a particular wavelength.

$$R(\lambda) = \frac{I(\lambda)}{P(\lambda)} \tag{6}$$

where $P(\lambda)$ is the incident light power onto the device active area at a particular wavelength, and $I(\lambda)$ is the output photocurrent generated by the incident light at this wavelength.

1.5.3 External Quantum Efficiency

External quantum efficiency is the number of collected carriers divided by the number of the incident photons per unit time, and it can be converted from responsivity directly at any particular wavelength as follows.

$$EQE(\lambda) = \frac{hc * R(\lambda)}{q\lambda} = \frac{1.24 * R(A/W)}{\lambda(\mu m)} \quad (7)$$

where h is the Planck constant, c is the speed of light, and q is the elementary charge.

1.5.4 Noise

Noise N is defined as the root mean square (RMS) deviation of the total output current (if the incident light signal is DC), which is dependent on the central frequency of the band pass filter (BPF) and the bandwidth of the BPF Δf. N is proportional to $\sqrt{\Delta f}$. There are various kinds of noise in the photodetector such as shot noise, Johnson noise and 1/f noise.

Noise spectral density n is defined as $N/\sqrt{\Delta f}$, which is independent of the bandwidth, and can be a function of frequency. In most cases, the n is dominated by 1/f noise in the low frequency regime, and is dominated by frequency-independent white noise at high frequency regime.

1.5.5 Detectivity

Detectivity is defined as the ratio of the responsivity over the noise, which is dependent on the device area and bandwidth.

$$D(\lambda) = \frac{R(\lambda)}{N} \tag{8}$$

where the N is the noise of the photodetector.

1.5.6 Specific Detectivity

Specific Detectivity (D*) is a normalized detectivity which is independent on the device area and bandwidth. Therefore, it is the ultimate specification to compare photodetectors with different device area and bandwidths. The higher the D* is, the better the photodetector is. The D* has a unit of cm-Hz$^{1/2}$/W or Jones.

$$D^{*}(\lambda) = \frac{R(\lambda)\sqrt{S}}{N/\sqrt{\Delta f}} = \frac{R(\lambda)\sqrt{S}}{n} \tag{9}$$

where R is responsivity, S is the total area of the photodetector, N is noise, Δf is the bandwidth. Good MWIR and LWIR photodetectors typically have a D^* over 10^{12} cm-Hz$^{1/2}$/W and over 10^{11} cm-Hz$^{1/2}$/W respectively at 77 K.

II MWIR NBN PHOTODETECTORS USING INAS/INASSB TYPE-II SUPERLATTICE

2.1 Chapter II Introduction

As discussed in Chapter 1.1, InAs/InAsSb type-II superlattices (T2SL) have very long carrier lifetime of >412 ns [11], and nBn photodetectors are capable of suppressing the dark current. Therefore, it is reasonable to expect that an nBn photodetector based on InAs/InAsSb T2SL has potentially high device performance. In 2012, a 13.2 μm cutoff LWIR nBn photodetector based on InAs/InAsSb T2SL was demonstrated with a very low dark current of 5×10^{-4} A/cm^2, at 77 K under a bias of -0.3 V [31]. The low dark current was attributed to the long minority carrier lifetime, low hole mobility of the InAs/InAsSb T2SL absorber [42], and the unintentional valence band bump in the barrier layer [43]. However, the single-pass EQE at 77 K and at 12 μm detection wavelength, is only 2.5 % [31], due to the low absorption coefficient of ~ 300 cm^{-1}, short diffusion length of ~ 0.9 μm [42], and the unintentional valence band bump in the barrier layer. As a result, even though the dark current is low, due to the low EQE, this LWIR InAs/InAsSb T2SL nBn photodetector has a low calculated specific detectivity of 10^{10} cm-Hz$^{1/2}$/W.

To enhance the detectivity of the LWIR InAs/InAsSb T2SL nBn photodetector, it is vital to increase the absorption coefficient and hole mobility of the InAs/InAsSb T2SL, and to make the valance band edge more aligned. The former can be realized by shortening the period of the InAs/InAsSb T2SL and the latter can be achieved by controlling the band position of the barrier layer more precisely to ensure it is well aligned with that of the InAs/InAsSb T2SL. To shorten the period, it is vital to increase the Sb composition for maintaining both the LWIR band gap and the strain balancing. In

2014, a LWIR InAs/InAsSb T2SL nBn photodetector with a shorter period of 8.6 nm InAs / 2.2 nm $InAs_{0.45}Sb_{0.55}$ was demonstrated [32], whose period is only half of the 13.9 nm InAs / 4.5 nm $InAs_{0.62}Sb_{0.38}$ of the previous smallest reported in 2012. On the other hand, a barrier layer design of 6/2/6/7 monolayers of InAs/AlAs/InAs/$InAs_{0.45}Sb_{0.55}$ per period is chosen to ensure a better valence band edge alignment. This LWIR InAs/InAsSb T2SL nBn photodetector reported in 2014 has an enhanced EQE of 15 %, at 77 K, and a 10 µm detection wavelength with an absorber thickness of 2 µm, and the calculated specific detectivity is an enhanced 2.8×10^{11} cm-$Hz^{1/2}$/W [32].

This work focuses on MWIR InAs/InAsSb T2SL nBn photodetectors, with a short period of 5.24 nm InAs / 4.76 nm $InAs_{0.81}Sb_{0.19}$ that ensures large absorption coefficient and high hole mobility, and a low Sb composition of 0.19 which enables better growth reproducibility. Furthermore, this MWIR 5.2 nm InAs / 4.7 nm $InAs_{0.81}Sb_{0.19}$ T2SL has shown a long carrier lifetime of 1.26 µs at 77 K, at which the adverse carrier localization effect is weak [12], suggesting superior material quality and the potential to achieve high device performance. In the following chapters, the design, growth, processing, and characterization will be discussed throughout for a series of nBn photodetectors based on MWIR InAs/InAsSb T2SL, with different absorber doping concentrations from 10^{16} cm^{-3} to 10^{18} cm^{-3}, and various absorber thicknesses from 1 µm to 2.5 µm.

2.2 MBE Growth and Device Processing

The nBn photodetectors are grown on undoped (100) 2-inch GaSb substrates using a VG V80 solid-source MBE system. As the layer structure in Figure 14, the growth starts with a 500-nm-thick GaSb buffer at 500 °C, followed by the bottom contact

layer consisting of 100 periods of 5.24 nm InAs:Si (3×10^{18} cm^{-3}) / 4.76 nm $InAs_{0.8}Sb_{0.2}$ T2SL layers. Next, a 250-period un-intentionally doped 5.24 nm InAs / 4.76 nm $InAs_{0.8}Sb_{0.2}$ T2SL absorber layer is grown, followed by a barrier consisting of 20 periods of 2.93 nm InAs / 2.17 nm $Al_{0.94}Ga_{0.06}As$ T2SL layers. Finally, the n-type top contact layer is grown, which consists of 10 periods of 5.24 nm InAs:Si (1×10^{19} cm^{-3}) / 4.76 nm $InAs_{0.8}Sb_{0.2}$ T2SL layers, and then a 30 nm InAs:Si (1×10^{19} cm^{-3}) top layer (see Figure 14). The growth temperature is kept at 400 °C during the growth of all superlattice layers. To grow nBn samples with other doping concentrations and absorber thicknesses, the Si doping flux and periods of the T2SL absorber layers are adjusted.

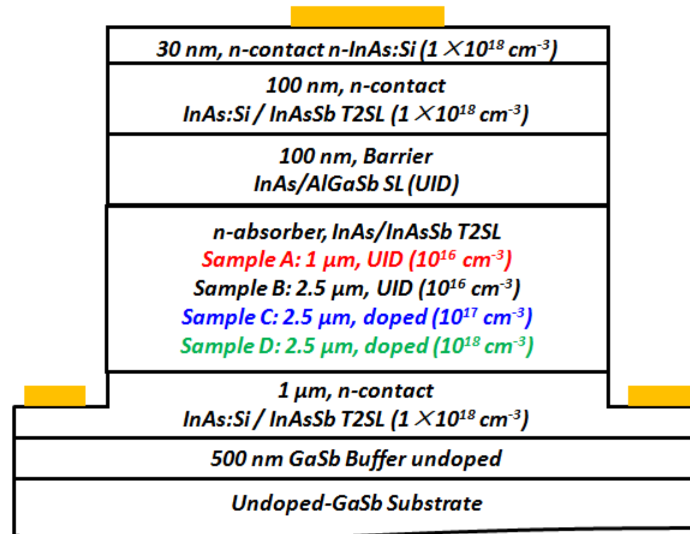

Figure 14 Cross section schematic of the MWIR InAs/InAsSb T2SL nBn detector samples fabricated at ASU, with different doping concentrations and thicknesses of the absorber region.

Device processing starts with photolithography to define the mesas with a size of 400×400 μm^2. First, the InAs/InAsSb T2SL top layer and the InAs/AlGaSb T2SL barrier layer was etched using phosphoric acid: H_2O_2 solution: DI water with a volume ratio of 1: 1: 10. Then, citric acid solution (1 g citric acid: 1 mL water): H_2O_2 solution with a volume ratio of 50:1 was used to obtain a smooth mesa sidewall, and uniform etching depth. The etching was stopped at the middle of the bottom n-type InAs/InAsSb T2SL contact layer. Both of the top and the bottom Ohmic contacts are 50 nm Ti / 50 nm Pt / 300 nm Au. The top contact is a circular metal pad at the center of the mesa top with a diameter of 200 μm, and the bottom contact is a large 400 μm × 5 mm strip deposited at the surface of the bottom InAs/InAsSb T2SL contact layer. Ti is used as the first metal to directly touch the T2SL due to its good bonding to the T2SL material and its ability to avoid peeling-off during the wire-bonding. No surface passivation or anti-reflection coatings were applied. The external bias is applied to the top contact of each mesa, and the bottom contact is always grounded.

2.3 Device Characterization

2.3.2 Characterization Methods

To measure the specifications as discussed in Chapter 1.4 for infrared photodetectors, special methods need to be used and they will be discussed in details in this chapter. First, the dark current characteristics of infrared photodetectors are measured with a thermal shield covering the sample hold. This thermal shield can block the background infrared radiation from the lab and it is cooled down to cryogenic temperature to minimize the infrared radiation from itself. Then, the

wavelength-dependent photocurrent of the device under test (DUT) can be directly measured using a Fourier transform infrared spectroscopy (FTIR) system with an internal infrared light source whose power spectrum is known. Then, an uncalibrated responsivity spectrum of the DUT with arbitrary responsivity units can be calculated. Afterwards, to calibrate the responsivity spectrum of the DUT, a standard blackbody light source with a spectrum strictly following Planck's law is used to illuminate the device. Using a lock-in amplifying technique, the photocurrent of the DUT under the blackbody with a known power can be measured. The responsivity spectrum of the DUT can be then be calibrated using this measured photocurrent. At last, the D* spectrum of the DUT can be calculated after the noise spectral density of the DUT is measured using a lock-in amplifier or an electrical spectrum analyzer. In addition, more in-depth device studies can be carried out by measuring the dependence of the specifications on other variables, such as device temperature, applied bias, light power and pixel areas.

2.3.2.1 Blackbody Responsivity

To measure the photocurrent under the illumination of a calibrated blackbody, a lock-in amplifying technique is used to filter out the dark current and the ambient photocurrent. A diagram of the experimental set-up is shown in Figure 15. The blackbody radiation, described by Planck's law, generates photocurrent in the DUT; mounted inside a cryostat cooled by a Helium compressor (this setup is capable of reaching temperatures at low as 12 K). The incident light is modulated mechanically by a chopper that is synchronized with a SR830 lock-in amplifier at a modulation frequency of 100 Hz. An SR570 transimpedance pre-amplifier is connected directly to the DUT, which applies a

DC voltage bias to the DUT, receives current signal from the DUT, converts the current signal to voltage signal, amplifies the signal, and sends the signal to the lock-in amplifier. The RMS value of the signal fundamental component at the modulation frequency can be read out using the lock-in amplifier.

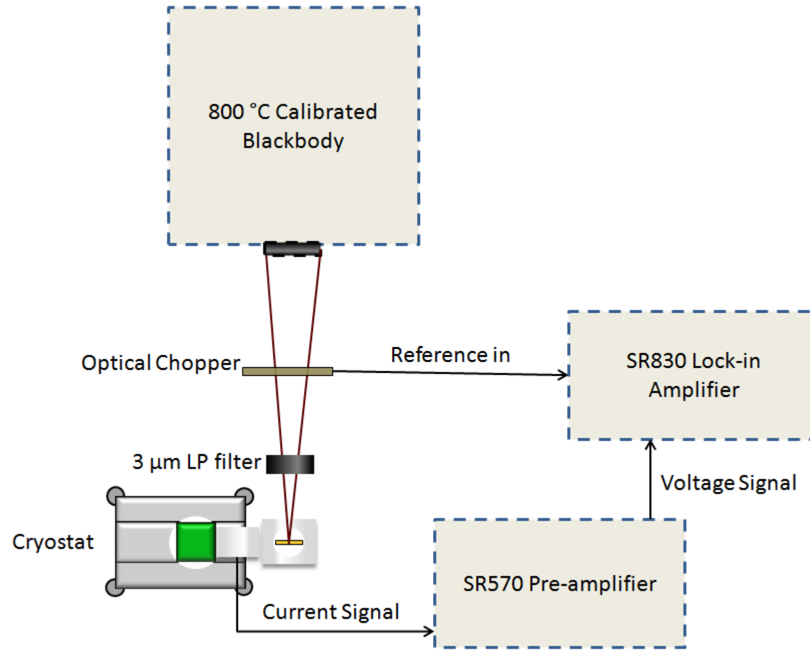

Figure 15 Block diagram of the setup to measure blackbody responsivity.

The photocurrent can be then calculated by:

$$I_{Photo} = \frac{(Lockin\ \ Reading) * (Preamplifier\ \ Sensitivity)}{Modulation\ \ Factor}$$

where the modulation factor is defined as:

$$MF = \frac{rms\ \ of\ \ fundamental\ \ components}{peak - to - peak\ \ value\ \ of\ \ total\ \ waveform}$$

It is important to note that a proper sensitivity of the pre-amplifier must be chosen so that the input impedance of the pre-amplifier is much less than the detector resistance.

Otherwise, the bias applied on the detector would be oscillating at a synchronized frequency with the incident light. This synchronized bias oscillation would cause a dark current oscillation at the modulation frequency and hence, result in a false photocurrent reading lower than the true value. In addition, the cutoff frequency of the sensitivity mode should be at least 100 times higher than the modulation frequency to avoid photocurrent signal degradation, and the current limit of the sensitivity mode should be higher than the DUT current to avoid overloading of the pre-amplifier.

The modulation factor (MF) can be looked up in the table of Figure 16 and it is dependent on many factors, such as the distance between the blackbody aperture and the DUT, the distance between the chopper and the DUT, and the geometry features of the chopper. As in Figure 16, the MF is determined by the number of tooth-slot pairs on the chopper, and the DAP/TW ratio that means the blackbody aperture diameter divided by the chopper tooth width projected on the same plane. Figure 16 is only valid for choppers with circular motion and radial teeth, and in the case that the DUT has an area much smaller than the blackbody aperture and the chopper blade has a negligible thickness.

Table 3.8 Modulation factors

DAP/TW	CASE III: NUMBER OF TOOTH-SLOT PAIRS				
	50	20	10	5	2
0.00	0.4502	0.4502	0.4502	0.4502	0.4502
0.10	0.4488	0.4488	0.4488	0.4488	0.4488
0.20	0.4446	0.4446	0.4446	0.4446	0.4446
0.30	0.4378	0.4378	0.4378	0.4378	0.4377
0.40	0.4283	0.4283	0.4283	0.4282	0.4279
0.50	0.4163	0.4163	0.4163	0.4162	0.4154
0.60	0.4020	0.4020	0.4019	0.4017	0.4002
0.70	0.3855	0.3854	0.3853	0.3850	0.3821
0.80	0.3670	0.3669	0.3668	0.3662	0.3613
0.90	0.3467	0.3466	0.3464	0.3454	0.3377
1.00	0.3249	0.3248	0.3244	0.3231	0.3113
1.10	0.3018	0.3017	0.3012	0.2993	0.2822
1.20	0.2777	0.2775	0.2769	0.2744	0.2502
1.30	0.2529	0.2527	0.2519	0.2487	
1.40	0.2276	0.2273	0.2264	0.2224	
1.50	0.2022	0.2018	0.2007	0.1959	
1.60	0.1768	0.1764	0.1751	0.1694	
1.70	0.1518	0.1514	0.1499	0.1435	
1.80	0.1274	0.1270	0.1253	0.1183	
1.90	0.1039	0.1034	0.1016	0.0942	
2.00	0.0815	0.0809	0.0791	0.0715	
2.10	0.0603	0.0598	0.0579	0.0507	
2.20	0.0405	0.0400	0.0383	0.0319	
2.30	0.0224	0.0219	0.0204	0.0155	
2.40	0.0059	0.0055	0.0043	0.0017	
2.50	-0.0087	-0.0090	-0.0098	-0.0093	
2.60	-0.0215	-0.0216	-0.0218	-0.0173	
2.70	-0.0324	-0.0323	-0.0318	-0.0223	
2.80	-0.0414	-0.0411	-0.0397	-0.0243	
2.90	-0.0484	-0.0479	-0.0455	-0.0235	
3.00	-0.0537	-0.0528	-0.0493	-0.0202	
3.10	-0.0571	-0.0560	-0.0512	-0.0152	
3.20	-0.0589	-0.0574	-0.0513		
3.30	-0.0591	-0.0573	-0.0499		

DAP = aperture diameter
TW = tooth width (along arc for case III)

Program AMODF - revised 9 Sept 1988 - JDV

Case III: radial teeth, circular motion, circular aperture

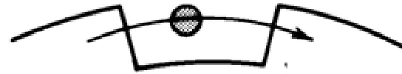

Figure 16 The modulation factors for different chopping conditions using a circular blackbody aperture and a chopper with radial teeth in circular motion [44].

The blackbody aperture is far away from the DUT (for instance 1-meter aperture/DUT distance, with 1-inch aperture diameter), the aperture plane is in parallel with the DUT plane, and therefore normal light incidence is satisfied. The incident power

in Watts on the photodetector from the 800 °C calibrated blackbody can be calculated by Equation (10).

$$P_{Blackbody} = TS_{active} \frac{\pi r^2}{d^2} \int_{\lambda 1}^{\lambda 2} B(\lambda) d\lambda \tag{10}$$

where T is the transmission rate of the cryostat window (0.7 for ZnSe), $B(\lambda)$ is the spectral radiance of the calibrated blackbody, with units of $W/\mu m/sr/cm^2$, λ_1 and λ_2 are the cutoff wavelengths of the band-pass filter, r is the radius of the blackbody aperture, d is the distance between the DUT and the blackbody aperture and S_{active} is the active area of the DUT (which means the window area unblock by the top metal contact).

As shown in Equation (5), the blackbody responsivity is the measured photocurrent divided by the calculated blackbody light power as in Equation (10).

2.3.2.2 Spectral Responsivity

A normalized spectral responsivity $f(\lambda)$ with a peak value of 1 can be obtained by measuring the spectral photocurrent of the DUT, under the internal light source of a FTIR spectrometer. The $f(\lambda)$ is the photocurrent spectrum divided by the power spectrum of the internal light source that can be calibrated using a commercial HgCdTe photodetector. Using the measured blackbody responsivity, as in Chapter 2.3.2.1, the spectral responsivity can be calculated as follows:

$$R(\lambda) = R_{Blackbody} \times PF \times f(\lambda) \tag{11}$$

where $R_{Blackbody}$ is the measured blackbody responsivity, and PF is the peak factor that can be calculated as follows:

$$PF = \frac{\int_{\lambda 1}^{\lambda 2} B(\lambda) d\lambda}{\int_{\lambda 1}^{\lambda 2} f(\lambda) B(\lambda) d\lambda} \quad (12)$$

where $B(\lambda)$ is the spectral radiance of the calibrated blackbody with a unit of $W/\mu m/sr/cm^2$, λ_1 and λ_2 are the cutoff wavelengths of the band-pass filter.

2.3.2.3 Noise

Noise is defined as the standard deviation of the dark or ambient current under a DC bias within a certain bandwidth. Noise spectral density is the noise divided by the square root of the bandwidth. The noise spectral density at a certain frequency can be read out directly from the X_{noise} output of the SR830 lock-in amplifier, and it has units of $V/Hz^{1/2}$. The internal frequency of the SR830 lock-in amplifier can be adjusted to measure the noise spectral density at different frequencies. By changing the time constant of SR830 lock-in amplifier, the bandwidth is changed and so is the noise spectral density reading, unless the noise is a white noise. To measure white noise spectral density, an internal frequency of 10 kHz on the lock-in amplifier is usually chosen, which is high enough to be far away from the low-frequency 1/f noise range, and low enough to avoid the upper bound cut-off frequency of 1 MHz limited by the pre-amplifier. Alternatively, the noise spectral density as a function of the frequency can be more straightforwardly measured by an electoral spectrum analyzer, in which the noise spectral density vs. frequency curve is clearly shown in real time, and the 1/f noise can be better characterized.

As in Equation (13), to measure the noise spectral density originating from the DUT, it is necessary to subtract the system noise spectral density that may originate from the instrument, cables, and background in the lab.

$$n_{detector} = \sqrt{n_{total}^2 - n_{system}^2} \tag{13}$$

Total noise spectral density is measured with the chopper switched off and the blackbody aperture blocked, as in Figure 17. To measure the system noise spectral density, everything is kept the same as in Figure 17 except the cable is disconnected between the detector and the pre-amplifier.

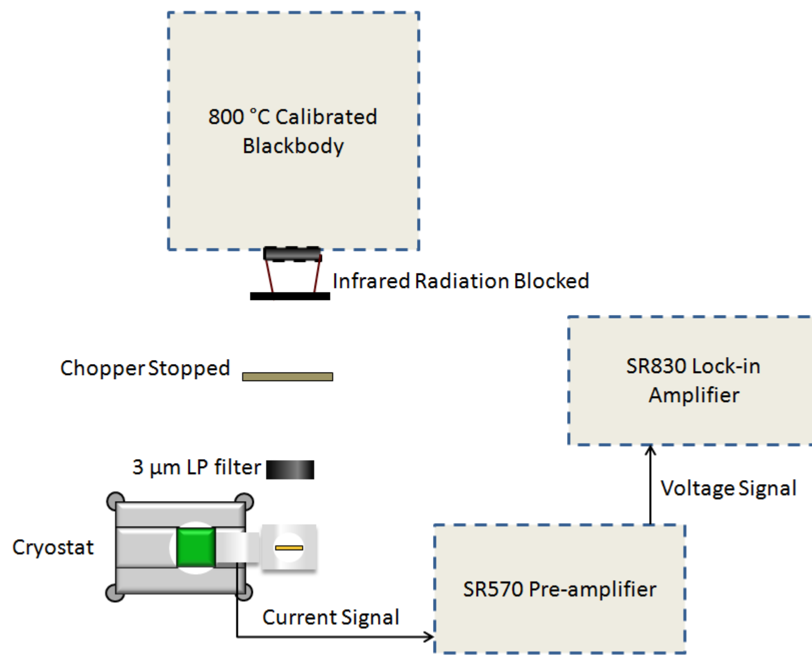

Figure 17 Block diagram of the setup used to measure the detector noise.

*2.3.2.4 Spectral D**

Once the spectral responsivity *R(λ)* and noise spectral density *n* have been measured, the spectral specific detectivity can be calculated by:

$$D^*(\lambda) = \frac{R(\lambda)\sqrt{S}}{n} \tag{14}$$

where *S* is the total pixel area of the photodetector.

Alternatively, if the system noise is too high to resolve the DUT noise, the white noise spectral density can be calculated using the measured dark or ambient I-V curves, and the spectral D* can be calculated using Equation (15), assuming Johnson noise and shot noise are dominant.

$$D^*(\lambda) = \frac{R(\lambda)\sqrt{S}}{\sqrt{4kT/r + 2qI}} \tag{15}$$

where *R* is the measured responsivity, *S* is the mesa area, *k* is Boltzmann constant, *T* is the temperature, *r* is the measured differential resistance of the device, *q* is the elementary charge, and *I* is the measured dark or ambient current of the device.

2.3.3 Dark Current

2.3.3.1 Single-element nBn

Single-element nBn means nBn pixels defined by etch stopped at the bottom contact layer, and therefore the absorber layer has a sidewall exposed to air. As in Figure 19, dark I-V curves of single-element MWIR InAs/InAsSb T2SL nBn photodetectors without any surface passivation were measured at a probe station at 77 K. Compared to single-element PIN photodetectors using similar MWIR InAs/InAsSb T2SLs with no

surface passivation, the nBn photodetectors show over 10^5 times smaller dark current under –0.2 V at 77 K. This is attributed to the effective blockage of the surface conduction channel by the barrier layer of the nBn.

Figure 18 Layer structures of the MWIR nBn and PIN photodetectors based on InAs/InAsSb T2SLs, in both of which the absorbers are unintentionally doped as n-type and are around 2.5 μm thick.

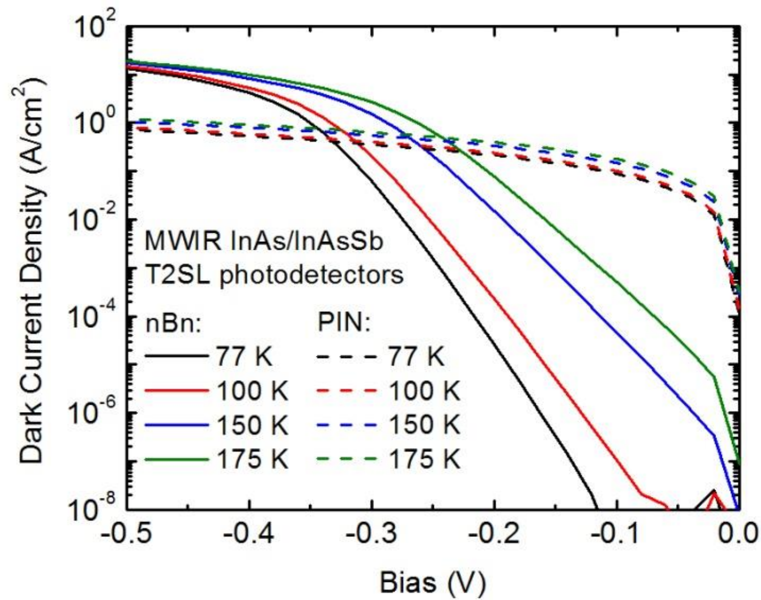

Figure 19 Dark current is greatly suppressed in the nBn photodetector compared to the PIN photodetector based on MWIR InAs/InAsSb T2SLs.

2.3.3.2 Shallowly Etched nBn

Shallowly etched nBn photodetectors are defined by etching selectively stopped at the top surface of the barrier layer (dark blue), as shown in Figure 20. The selective etchant is citric acid solution (1 g citric acid: 1 mL DI water): H_2O_2: water solution with a volume ratio of 1: 1: 10. It etches the InAs/InAsSb T2SL only, and does not etch the InAs/AlGaSb(As) T2SL. Shallowly etched nBn photodetectors have no sidewall effect because there is no sidewall on the absorber layers. I-V curves in Figure 20 show that the shallowly etched and the single-element nBn photodetectors have similar dark I-V curves, which suggests that exponentially increasing dark current is not caused by the surface but by effects in the bulk material.

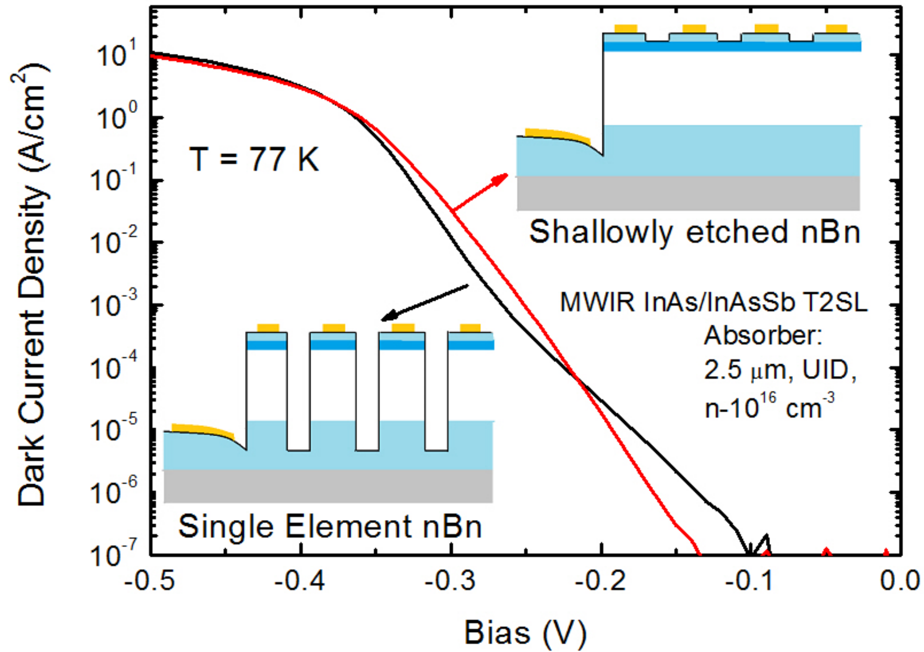

Figure 20 Dark I-V curves and cross section schematics of shallowly etched nBn vs single element nBn detectors.

*2.3.4 Responsivity and D**

2.3.4.1 Spectral Responsivity

The voltage dependence of the responsivity and the normalized responsivity spectrum are plotted in Figure 21 It is observed that the normalized responsivity spectrum is the same under different voltage biases. Under low biases smaller than −0.2 V, even though the dark current is suppressed to be lower than 2×10^{-5} A/cm^2, the responsivity is smaller than 0.05 A/W. To turn on the responsivity to be greater than 1 A/W, it is necessary to apply a bias greater than −0.3 V. However, under such a high bias, the dark current is higher than 0.1 A/cm^2 which induces high shot noise and Johnson noise. It is found that under a bias of −0.3 V, the calculated specific detectivity (D*) of the device reaches a maximum of 5×10^9 cm-Hz$^{1/2}$/W, which is much lower than the calculated

8×10^{12} cm-Hz$^{1/2}$/W in a MWIR nBn photodetector using a similar InAs/InAsSb superlattice absorber, but having a better aligned valence band [38].

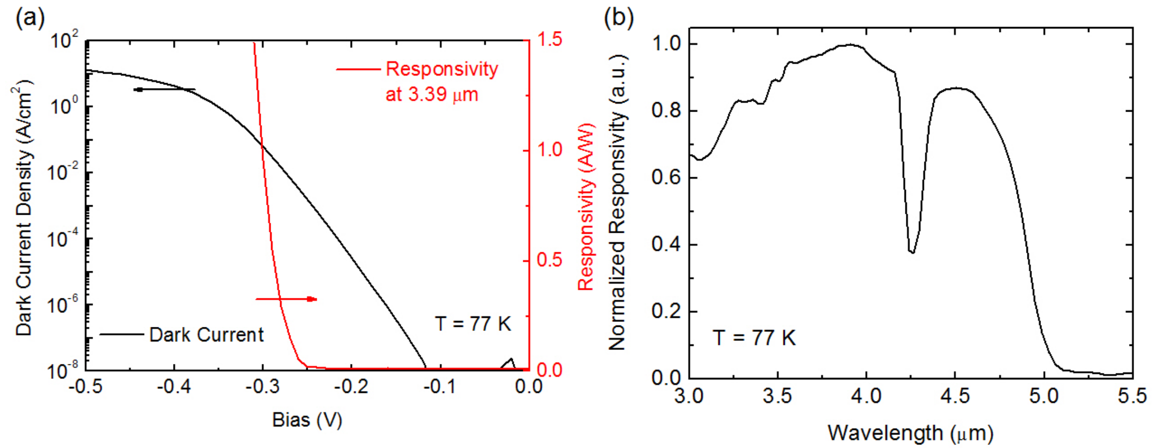

Figure 21 (a) Dark current and responsivity at the wavelength of 3.39 μm as functions of the applied bias at the temperature of 77 K (b) Normalized responsivity spectrum at 77 K in the MWIR InAs/InAsSb superlattice nBn photodetectors.

*2.3.4.2 Spectral D**

The spectral D* of samples with different doping concentrations and identical absorber thicknesses of 2.5 μm at 77 K are shown in Figure 22. Biases applied to the devices are optimized to achieve the highest possible D* values. X-ray diffraction (XRD) shows that the two samples with different absorber doping concentrations of 10^{17} cm^{-3} and 10^{18} cm^{-3} , have the same period of 5.1 nm InAs / 4.6 nm $InAs_{0.85}Sb_{0.15}$. However, the one with 10^{18} cm^{-3} absorber doping concentration has a shorter cutoff wavelength. This blue shift of the cutoff wavelength as the doping concentration increases is due to the Moss-Burstein effect [45][46]. It is found that the 10^{17} cm^{-3} doped sample has the highest

D* of 1×10^{11} cm-Hz$^{1/2}$/W at a wavelength of 4 μm. This suggests that doping in the absorber region can help achieve a higher D*, but too much doping, for example 10^{18} cm^{-3}, can lead to degradation of the D*, because there are more recombination centers and a lower carrier mobility in the absorber induced by the doping atoms. However, the highest D* of 1×10^{11} cm-Hz$^{1/2}$/W is still lower than the expected value of 8×10^{12} cm-Hz$^{1/2}$/W as reported for a MWIR nBn photodetector based on InAs/InAsSb superlattice [38], which is due to the high dark current as measured in Chapter 2.3.3. The cause for the high dark current is explored in the following chapter.

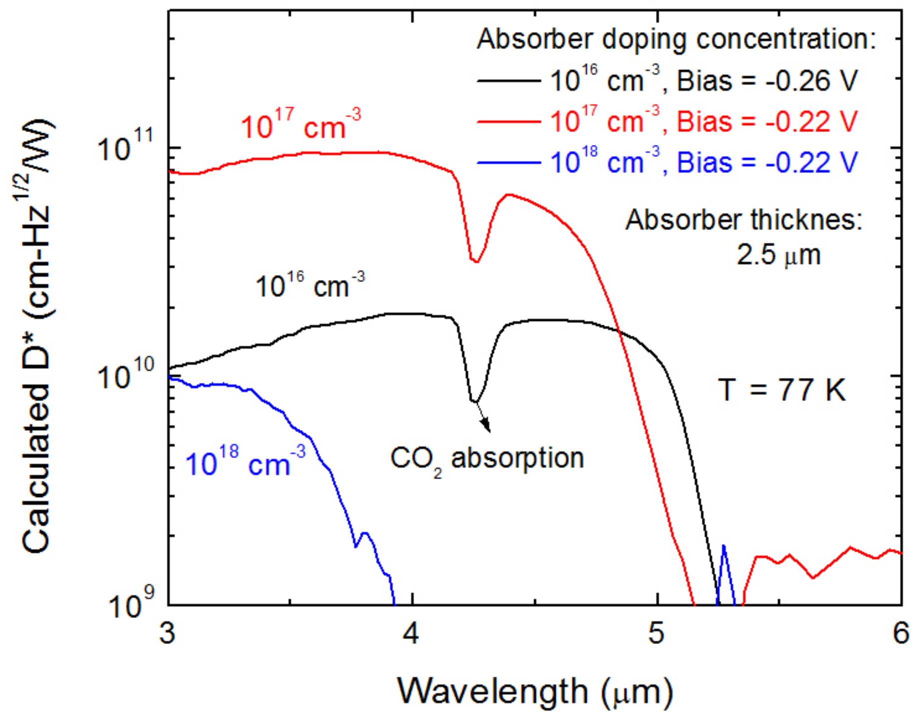

Figure 22 Specific detectivity spectra at 77 K for 2.5 μm thick devices with different absorber doping concentrations.

2.3.5 Charge Storage

2.3.5.1 Type-II Bandedge Alignment

A type-II bandedge alignment of the barrier layer and the absorber layer, as in Figure 23, is suggested through off-axis electron holography measurements at room temperature. The voltage profile of the cross-section shows the presence of positive charge with an estimated density of 1.81×10^{17} cm^{-3} in the barrier layer at room temperature [43]. This positive change is not due to ionized donors in the unintentionally-doped barrier layer because no positive charge is observed in the unintentionally-doped InAs/AlGaSb(As)-superlattice barrier layer of a similar nBn photodetector grown in the same chamber, in which the absorber layer and the barrier layer have a type-I bandedge alignment [43]. As a result, the observed positive charge at room temperature is attributed to trapped and accumulated holes in the barrier layer, indicating the presence of a potential well in the valence band of the barrier layer.

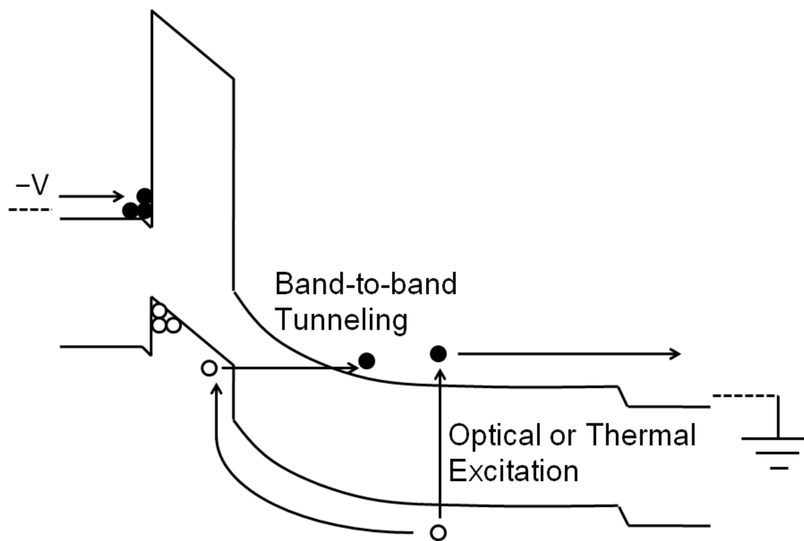

Figure 23 A schematic bandedge diagram of the devices under a negative bias. The carriers are generated by either optical or thermal excitation in the absorber, or electron band-to-band tunneling from the barrier layer to the absorber layer. Due to the type-II bandedge alignment, the electrons and holes get accumulated at the top-contact-layer/barrier-layer interface.

The potential well in the valence band is further confirmed by the observed exponentially increasing dark current as in Figure 20. As our device simulation suggests, the dark current should saturate if the valence bandedge was aligned or has a bump. By contrast, if the bandedge alignment is type-II as in Figure 23, the electrons can easily tunnel from the barrier-layer valence band to the absorber-layer conduction band, with a much lower triangular tunneling barrier than that if the valence bandedge was aligned or has a bump. On the other hand, the carrier recombination current and hole thermionic emission current at the top-contact-layer/barrier-layer interface increases exponentially as the bias increases. These two processes connected in series cause the exponentially increasing dark current.

The observed low D* as in Chapter 2.3.4 can be explained by the potential well in the valence band of the barrier layer. At low biases smaller than −0.3 V, the well traps the photogenerated holes and the responsivity is too low even though the dark current is low. Whereas at high biases greater than −0.3 V, band-to-band tunneling current is triggered and the noise is too high even though the responsivity is high. Consequently, it is very difficult to achieve a high responsivity and low dark current at the same time if a

potential well is present in the valence band, and therefore the D* is much lower than the expected.

2.3.5.2 Charge Storage Time

Experimental evidence has suggested that, for the InAs/InAsSb superlattice nBn photodetectors with a potential well in the valence band of the barrier layer, photogenerated charge can be stored in the potential well. This charge storage effect has been observed for samples with shallowly etched mesa, under low bias ~ −0.2 V that ensures low dark current $<10^{-5}$ A/cm^2, by using photo-capacitance and photocurrent decay measurements.

Photo-capacitance decay measurement result is as shown in Figure 24. The measurement was conducted at -0.1 V and 16.5 K which ensure an extremely low dark current of 10^{-8} A/cm^2. The device is initially illuminated by a 3.39 μm CW laser with a power of ~ 1 mW, and then the laser beam is blocked with a partial blocking time shorter than 0.1 ms. It is observed that under the light, the device capacitance is enhanced by 0.39 pF, and after the laser beam is blocked, the capacitance drops abruptly first and then decays slowly with a time constant of about 40 s. This slow decay is not due to surface defect states given the absence of side-walls in the absorber layer and barrier layer, and instead it is attributed to the hole de-trapping processes from the potential well in the barrier layer. The de-trapping processes include hole thermionic emission from the potential well and electron-hole recombination at the type-II interfaces.

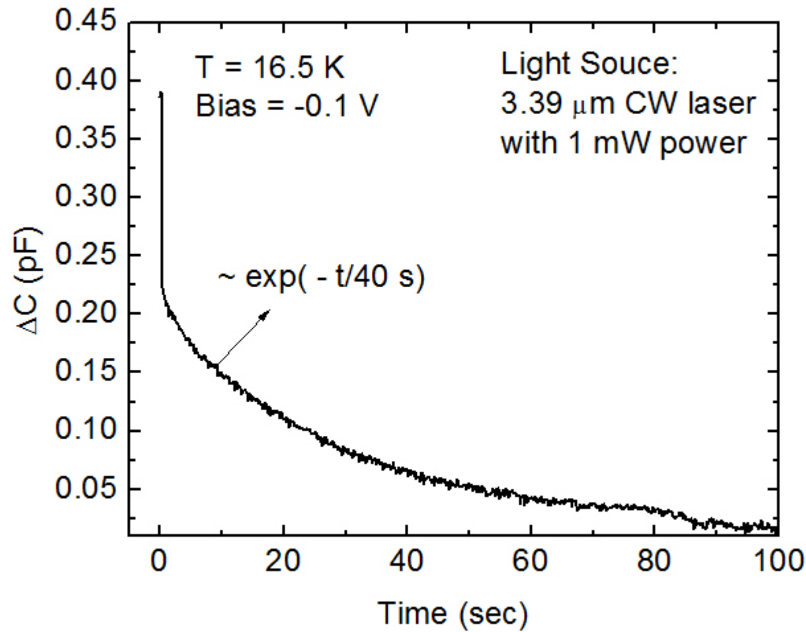

Figure 24 The capacitance is enhanced by 0.39 pF under light, which suggests the collection of the photogenerated holes by the barrier layer, and after the light is turned off, the capacitance decays slowly with a time constant of 40 s at 16.5 K under −0.1 V.

Furthermore, it is observed that the device current also has a long decay time after the light is turned off. Figure 25 shows the current decays at −0.25 V and 77.6 K. The current decays with a relatively short time constant of 5 s first, and then decays slowly with a long time constant of 60 s. Also, it is observed that, the slow decay part of the current has a nonlinear relation with the incident light power. As in Figure 25, By increasing the light power by 100 times from 0.05 mW to 5 mW, the slow decay part is enhanced by only 4.6 times from 0.045 μA to 0.206 μA. The long decay time of the current is also attributed to the slow hole de-trapping process from the potential well of the barrier layer. By contrast, this slow current decay is not observed in the MWIR PIN

photodetector based on an InAs/InAsSb superlattice without any heterostructure interfaces as in Chapter 2.3.3.1.

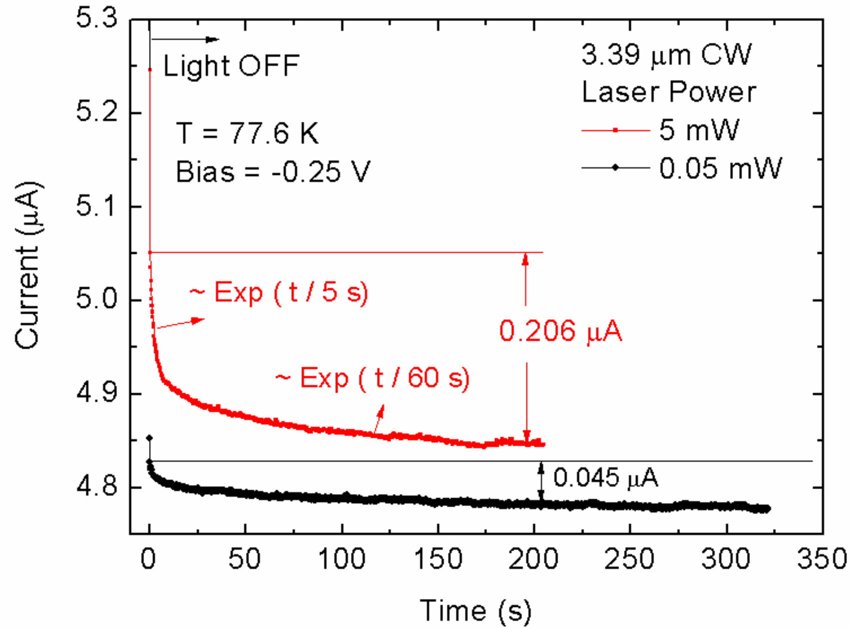

Figure 25 Current decay characteristic of the InAs/InAsSb nBn photodetector at 77.6 K, -0.25 V after light is turned off

In general, the observed long decay time of the capacitance and the current can be attributed to a low hole thermionic emission current from the potential well, and a long electron-hole recombination lifetime due to charge separation in space [48][49]. This long decay time suggests a long charge storage time in the potential well and indicates that it is possible to read out the stored charge before they vanish. As in charge coupled devices (CCD)[50], the stored charge can be readout laterally through transferring the charge between pixels in a focal plane array using multi-phase voltage clock. It is expected that such devices have greatly reduced noise for the following two reasons. On

the one hand, by accumulating the photogenerated holes in the barrier layer, the photocurrent signal is integrated over time and therefore the noise is suppressed significantly. This signal integration process in device level has a lower noise than that conducted in peripheral circuitry. On the other hand, a low voltage bias is required to collect the photogenerated holes due to the heterostructure potential well in the valence band. The low voltage ensures the absence of depletion in the absorber layer, and therefore low dark current and low noise.

2.4 Chapter II Summary

We have demonstrated MWIR nBn photodetectors based on InAs/InAsSb superlattices with a cut-off wavelength of 4.9 μm. The device growth, processing, and characterization are discussed comprehensively. It is observed that the highest sepecifity detectivity D* is $< 10^{11}$ cm-Hz$^{1/2}$/W, which is much lower than the expected $>5\times10^{12}$ cm-Hz$^{1/2}$/W at 77 K. After careful investigation, the low D* is attributed to the presence of a potential well in the InAs/AlGaSb(As) superlattice barrier layer. This potential well makes it very difficult to achieve both a high responsivity and a low dark current as the bias voltage varies, and therefore makes the D* low.

Even though the D* is low if photocurrent through top contact is treated as the output signal, experimental evidence has shown that it is possible that photogenerated charges are stored in the potential well and stored charges are treated as the output signal. At very low voltage bias smaller than -0.2 V, which ensures a dark current smaller than 10^{-5} A/cm^2, photogenerated holes can be collected and stored in the potential well of the barrier layer. A charge storage lifetime up to 40 s is determined by measuring the

photocurrent and photo-capacitance decay time after the light is turned off. Rather than being read out vertically via the top contact, this stored charge can be read out laterally along the barrier layer in the barrier layer in future devices. Such charge-output nBn photodetectors will not only leverage the advantage of conventional nBn photodetectors, such as a depletion-free absorber, but will also possess an in-pixel signal integration and averaging feature that can further reduce the random noise of infrared photodetectors.

III MONOLITHICALLY INTEGRATED VISIBLE/MWIR CDTE-NBN/INSB-PN TWO-COLOR PHOTODETECTORS

3.1 Chapter III Introduction

Compound semiconductors with a lattice constant near 6.5 Å, such as InSb, CdTe, MgTe, and HgTe have broad applications including photovoltaic and photodetection. For example, HgCdTe and InSb are widely used for infrared photodetectors [1]. Multi-crystalline CdTe are extensively applied for photovoltaic energy generation, with an energy conversion efficiency of 22.1% demonstrated [52], and single-crystalline CdTe and CdZnTe are broadly used for X-ray and gamma ray photodetectors [53].

Herein, we demonstrate monolithically-integrated visible/MWIR 2CPDs using lattice-matched CdTe and InSb sub-detectors, with cutoff wavelengths of 780 nm and 5.5 μm at 77 K, respectively. Recently, high-quality CdTe and CdTe/MgCdTe double heterostructures on lattice-matched InSb substrates have been demonstrated with minority carrier lifetimes of up to 3.6 μs, and interface recombination velocities of 1.2 cm/s [54][55][56][57], which suggests the potential to achieve photodetectors with high performance. However, due to the difficulty in doping CdTe to be p-type [58], the CdTe sub-detector of the 2CPD needs to possess a heterostructure to circumvent the difficulty in developing a high quality homojunction. This can be accomplished in one of two ways, utilizing a CdTe PN structure with an α-Si:H p-type layer and MgCdTe passivation layers [57], or by using a CdTe nBn structure with a ZnTe barrier layer [59]. On the other hand, InSb PN structures have been well developed and can be used as a simple InSb sub-detector within the 2CPD [60].

3.2 CdTe/InSb Tunnel Junction

To realize the monolithic integration of CdTe and InSb photodetectors, it is vital to achieve a highly conductive CdTe/InSb hetero tunnel junction to connect the sub-detectors. Two samples as in Figure 26 are grown, processed and characterized. They consist of an n-type CdTe layer doped by In with a concentration of 1×10^{18} cm^{-3}, and an n-type(p-type) InSb layer doped by Te(Be) with a concentration of 1×10^{18} cm^{-3} (1×10^{19} cm^{-3}). I-V measurements have shown that the n-CdTe/n-InSb and n-CdTe/p-InSb interfaces have resistances of 0.005 Ω-cm^2 and 0.04 Ω-cm^2, respectively at 80 K, as in Figure 26. These low resistances ensure negligible voltage drop at the CdTe/InSb interface of the monolithically integrated CdTe/InSb two-color phtodetectors, and can be attributed to the diffusion of the atoms at the interface. The In atoms from InSb diffuse into the CdTe and serve as an n-type dopant for CdTe, which causes a local high doping region and lowers the tunneling barrier significantly.

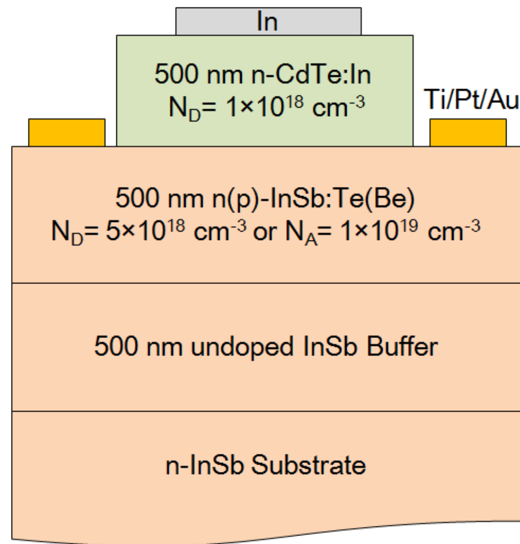

Figure 26 Device structure of the n-CdTe/n-InSb and n-CdTe/p-InSb tunnel junction samples.

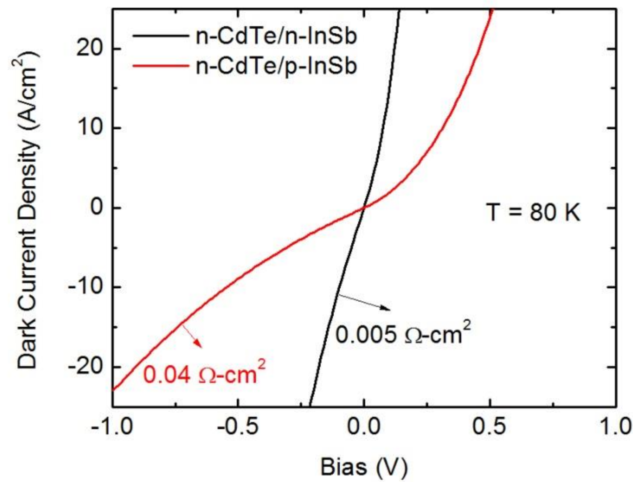

Figure 27 Dark I-V curves of the highly conductive n-CdTe/n-InSb and n-CdTe/p-InSb hetero tunnel-junctions at 77 K

3.3 Visible CdTe nBn Photodetector

3.3.1 Device Structure and MBE Growth

We here demonstrate a visible-to-NIR CdTe heterostructure nBn photodetector grown on an InSb substrate using molecular beam epitaxy (MBE). ZnTe is a simple and effective barrier layer for the CdTe nBn photodetector due to its near zero valence band offset of −0.05 eV, and large conduction band offset of 0.85 eV to CdTe, as revealed by X-ray photoelectron spectroscopy [61][62]. Even though the critical thickness of ZnTe on CdTe is only 1.6 nm, fully relaxed ZnTe layers with a film thickness of over 30 nm grown on CdTe using MBE show good crystalline quality [61]. The nBn structure circumvents the p-type doping difficulty for CdTe, and keeps the dark current as low as a CdTe PIN structure whose G-R dark current is already very low. Meanwhile, the nBn structure has a dark current lower than a Schottky diode, because the

majority-carrier-blocking heterostructure barrier in the nBn can be intentionally made thicker, and higher than the built-in barrier in the Schottky diode.

The CdTe nBn photodetectors were grown on an n-type 2-inch InSb (100) substrate with a doping concentration of 5×10^{17} cm^{-3} using a VG V80 solid-source MBE system. The layer structure is plotted in Figure 28(a). The growth of the CdTe nBn sample was started with the growth of a 500-nm-thick n-type InSb buffer layer (5×10^{18} cm^{-3}) at 390 °C, after thermal in-situ InSb oxide removal. Then the sample was transferred under ultra-high vacuum from the III-V to the II-VI chamber, where the 1-μm-thick CdTe layer with an indium doping concentration of 10^{18} cm^{-3} was grown. Next, a 1-μm-thick undoped CdTe absorber layer was grown, followed by an undoped ZnTe barrier layer with a thickness of 50 nm. Lastly, the 20 nm undoped CdTe top contact layer was grown. During the growth of the II-VI layers, the substrate temperature (measured by a pyrometer) started at 280 °C and then decreased to 265 °C due to changes in surface emissivity. After the growth, an ITO layer with a thickness of 70 nm was deposited as the top contact. Finally, a bottom Ohmic contact of Ti (20 nm) / Pt (20 nm) / Au (200 nm) was deposited on the back-side of the n-type InSb substrate. The band edge alignment of the CdTe nBn device is plotted in Figure 28(b).

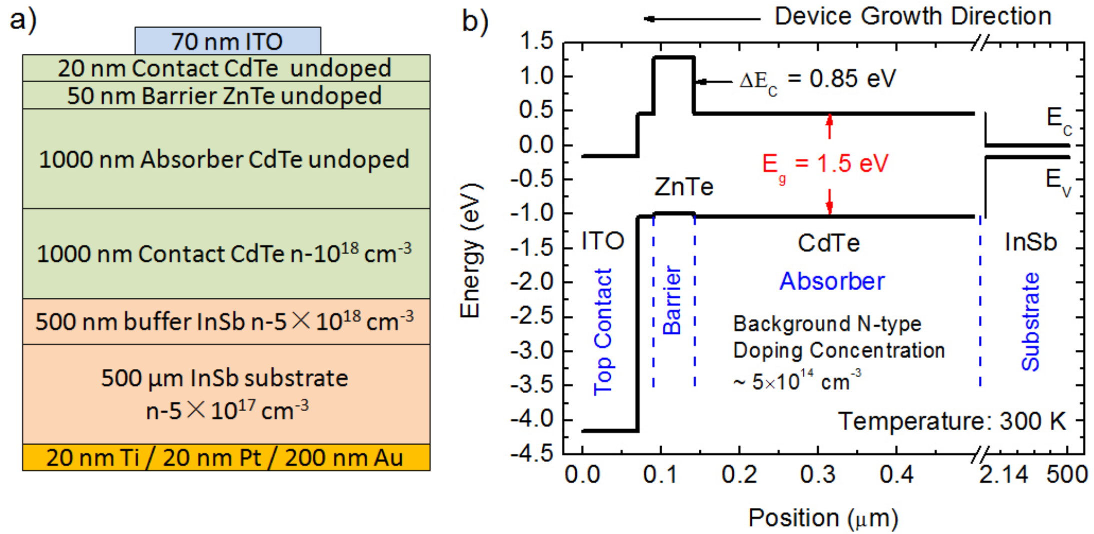

Figure 28 (a) Device layer structure of the CdTe nBn with a 1 μm thick CdTe absorber and a 50 nm thick ZnTe as the barrier layer. (b) Band edge alignment of the CdTe nBn photodetector.

ITO/undoped-CdTe is used as the top contact design for several reasons. First, the ITO is an anti-reflection coating that ensures a reflectance below 10% for the wavelength range from 450 nm to 800 nm. Second, since all the top undoped layers are nearly insulating, the top ITO contacts define the photodetector without any etching and eliminate any possible leakage current and carrier recombination on the side-wall surfaces if the photodetectors were etched into mesas. Third, experiments have shown that the top ITO/undoped-CdTe contact is a Schottky contact with a built-in electron barrier, which serves the purpose of the nBn structure design by allowing the holes to pass freely. Last, ITO/undoped-CdTe is an alternative, or an even better transparent conductive contact than the conventional metal/n-CdTe contact. On the one hand, the undoped CdTe layer ensures much lower electron thermionic emission current over the

barrier layer than a heavily doped n-type CdTe layer. On the other hand, experiments have shown that it is very difficult to dope the top CdTe on the ZnTe as n-type, because of high defect density caused by the lattice mismatch ZnTe layer.

3.3.2 Top Contact Optimization

The top contact of the CdTe nBn photodetector is optimized through trial and error as in Figure 29. In the first trial (Figure 29(a)), the top CdTe layer is doped as n-type using indium and an indium metal contact is deposited on the top, as in the conventional infrared nBn photodetectors. However, it was found that the n-type doping for the CdTe top contact layer on the lattice-mismatched ZnTe is difficult. In a control sample with a heavily indium-doped CdTe layer on ZnTe, even though the secondary ion mass spectrometry (SIMS) has confirmed an indium concentration of 10^{18} cm^{-3} in the top CdTe layer, the transmission line measurement (TLM) shows a near-insulating behavior (10^{9} Ω/sq) of the top CdTe layer, which suggests extremely low carrier concentration. This carrier freezing-out is attributed to the defects induced by the lattice-mismatch between the CdTe and ZnTe. It is reported [63] that for lattice-matched CdTe grown on InSb, a heavy indium concentration of 7×10^{18} cm^{-3} gives a carrier concentration of only 10^{17} cm^{-3}, which suggests the carriers can freeze out due to the defects induced by the indium doping. Due to the low carrier concentration in the top CdTe layer, even though the device in Figure 29(a) has a low dark current of ~ 10^{-9} A/cm^{2}, it shows a low EQE of only 25% due to the poor current spreading in the top CdTe layer.

In the second trial, as in Figure 29(b), the top CdTe layer and the indium contact are replaced by a layer of ITO to ensure good current spreading and optical transmission.

As expected, the EQE of this device is enhanced to be 80%. However, the dark current of this device is greater than 10^{-6} A/cm^2, which is at least three orders of magnitude higher than the first trial. The high dark current can be attributed to the built-in electron barrier of the ITO/ZnTe Schottky contact not being high, and thick enough to block the electron thermal emission current from the ITO contact.

In the third trial as in Figure 29(c), an undoped CdTe top contact layer with a thickness of 20 nm is added on the ZnTe barrier layer. This CdTe top layer provides a conduction band-edge kink to make full use of the ZnTe barrier layer. Compared to the second trial, the third trial has a thicker and taller heterostructure ZnTe barrier to block the electrons, than compared to the built-in electron barrier of the ITO/ZnTe Schottky contact. Finally, this device has shown both suppressed dark current of ~ 10^{-9} A/cm^2 and high EQE of 80%, which is the high-performance CdTe nBn photodetector discussed in Chapter 3.3.1.

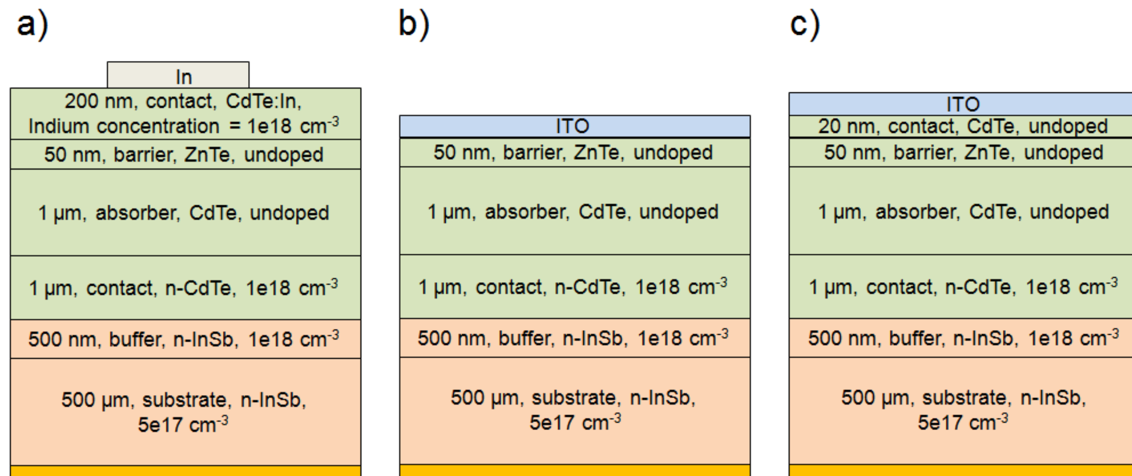

Figure 29 (a) CdTe nBn with heavily doped top contact layer and indium contact. (b) CdTe nBn with no top contact and ITO grown on the barrier layer directly. (c) CdTe nBn with the top contact layer and ITO top contact.

3.3.3 Dark Current and Responsivity vs. Voltage

The dark I-V characteristics of the CdTe nBn photodetector at room temperature are shown in Figure 30(a). The dark current is as low as 5×10^{-10} A/cm^2 under a bias of -0.1 V, reflecting a superior crystalline quality and the effectiveness of the nBn structure design. The responsivity vs. bias curve at the wavelength of 633 nm is also plotted in Figure 30(a). To collect the photogenerated holes in the absorber, it is necessary to apply a negative bias on the top contact. Under low negative bias, the depletion region is kept in the barrier layer. As the bias increases, the depletion region width increases and extends to the absorber layer. Therefore, the responsivity increases slowly as the bias increases. At a high bias of -3 V, the absorber is deeply depleted and the responsivity reaches 0.42 A/W, corresponding to an external quantum efficiency of 82%. This deep-depletion is similar to a charge-coupled device (CCD) [50], where it can be used to enhance the quantum efficiency, especially for near-band edge absorption with a low absorption coefficient, and to improve the spatial resolution if the device is used in a focal plane array (FPA) with ITO-defined pixels.

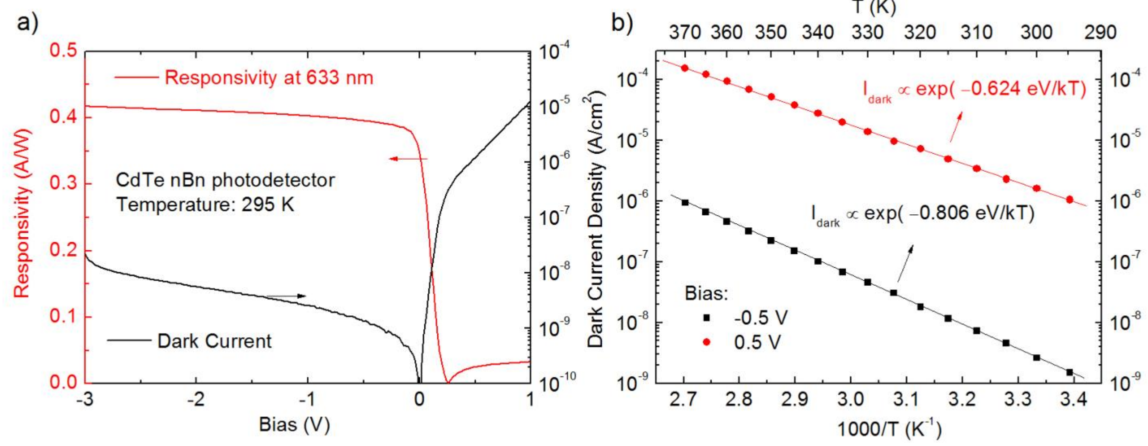

Figure 30 (a) I-V and responsivity-voltage characteristics at the wavelength of 633 nm at room temperature. (b) Arrhenius plot of the dark current as a function of temperature at -0.5 V and 0.5 V.

The bias dependent dark current behaviors in Figure 30(a) are explained as follows. The nBn device has a low dark current as the ZnTe barrier layer effectively blocks the majority carriers in the layers. C-V measurements for an undoped CdTe bulk material sample grown in the same chamber, under the same conditions, reveals an electron concentration of 5×10^{14} cm^{-3} due to the unintentional background dopants [63]. This result suggests a near-zero hole concentration of 10^{-2} cm^{-3}, given the intrinsic carrier concentration of CdTe is 10^{6} cm^{-3} at room temperature [64]. With the hole concentration of 10^{-2} cm^{3} and a hole mobility of 100 cm^{2}/V-s, the estimated direct hole drift current is below 10^{-15} A/cm^{2} under -0.5 V. Also, it is calculated that the electron tunneling current through the ZnTe layer is below 10^{-80} A/cm^{2}. Furthermore, detailed calculation suggests an electron concentration of 2.5×10^{16} cm^{-3} in the top CdTe layer under the bias of -0.5 V, which induces a thermionic emission current of 2×10^{-11} A/cm^{2} over the electron barrier of

the ZnTe layer. Clearly, the measured dark current of 10^{-9} A/cm^2 at -0.5 V is not dominated by any of the above effects. To clearly explain the origin of the dark current, a schematic diagram of the carrier G-R and transport processes in the CdTe nBn photodetector are shown in Figure 31. For instance, if a negative bias is applied on the top contact, as in Figure 31, the electrons are injected from the top contact into the conduction band of the top CdTe layer. Since the electrons are blocked by the conduction band barrier of the ZnTe layer, the continuation of current through the ZnTe layer is maintained through i) net electron-hole recombination in the top CdTe layer, ii) hole transport through the ZnTe layer via the valence band, and iii) net electron-hole generation in the CdTe absorber. Our simulations show that among the above three processes connected in series, the net thermal generation in the CdTe absorber is the current-limiting process. Accordingly, the dark current is dictated by the thermal, or Shockley-Read-Hall (SRH) net generation process in the CdTe absorber. In contrast, if a positive electrical bias is applied on the top contact, the dark current is dictated by the SRH net generation process in the top CdTe layer. As shown in Figure 30(a), the dark current at positive bias is more than three orders of magnitude higher than that under negative bias, because the top CdTe layer grown on the lattice-mismatched ZnTe has significantly more defects than the CdTe absorber which is grown on the lattice-matched InSb. A higher defect density induces higher SRH G-R current.

The dominance of G-R dark current from the CdTe layers is confirmed by temperature dependent measurements which reveal activation energies near half the bandgap energy of 0.75 eV, as shown in Figure 30(b). Furthermore, detailed calculations show the measured dark current corresponds to a SRH generation lifetime of 16 ns in the

depletion region, which is mainly due to the CdTe/ZnTe and the CdTe/InSb interface generation, rather than the generation in the bulk CdTe material. This is because CdTe materials with better interface grown in the same chamber, such as CdTe/MgCdTe double heterostructures have shown a long recombination lifetime of 3.6 μs, as measured by time resolved photoluminescence [57]. Similar single CdTe layers grown on InSb without MgCdTe barriers give poor photoluminescence and short recombination lifetimes, on the order of 10 ns, due to the recombination at CdTe surface and CdTe/InSb interface [65].

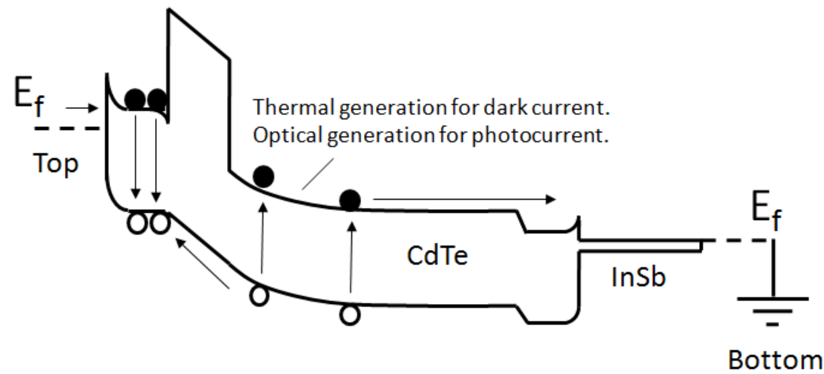

Figure 31 The schematic band diagram of the CdTe nBn photodetector under a negative bias applied to the top contact, and with the bottom contact grounded. The carrier generation-recombination and transport processes are shown.

The photocurrent has a similar bias-dependent behavior with the dark current because photogenerated carriers have to go through the same processes (Figure 31) as the dark current, except that the generation process in the absorber is realized by optical excitation rather than thermal excitation. Consequently, if a negative (positive) bias is applied on the top contact, the photocurrent signal exclusively originates from the photon

absorption in the absorber (top contact layer). This is the voltage-bias-addressed photodetection characteristic of nBn photodetectors. As in Figure 30(a), the saturated responsivity under negative bias in our device is 10 times as high as that under the positive bias. This can be attributed to the much thicker CdTe absorber (1 μm) than the top CdTe layer (20 nm), ensuring that the 633 nm light is absorbed dominantly by the CdTe absorber.

*3.3.4 Spectral Responsivity and D**

The spectral responsivity and external quantum efficiency are measured and plotted in Figure 32. The external quantum efficiency is higher than 70% from 550 nm to 800 nm, reflecting the aligned valence band edge of the CdTe and ZnTe layers, and the effective carrier collection of the ITO top contact layer. At 500 nm, the responsivity of the CdTe nBn photodetector is 3.3 times higher than the 0.075 A/W of a commercial GaAs PIN photodetector [66]. Such a high responsivity at short wavelengths can be attributed to the passivation effect of the ZnTe layer for the front surface of the CdTe absorber, which can suppress surface recombination greatly, especially of those carriers photogenerated by short-wavelength light with shallow penetration depths. However, in this specific CdTe nBn photodetector, the UV responsivity is not as high as expected due to the parasitic UV-absorption of the ITO layer and the top CdTe layer.

The specific detectivity (D*) spectrum is shown in Figure 33. A relatively flat D* plateau reaching 3×10^{13} cm-Hz$^{1/2}$/W that covers the visible range from 400 nm to 800 nm is demonstrated under a bias of -0.1 V at room temperature. This D* is close to those of the commercial Si, InGaAs, GaP and Ge photodiodes, which are ~10^{13} cm-Hz$^{1/2}$/W at -5

V or -10 V [67][68]. In the UV regime, the D* is around 1×10^{12} cm-Hz$^{1/2}$/W. The D* is calculated from Equation (15), assuming Johnson and shot noise is limiting.

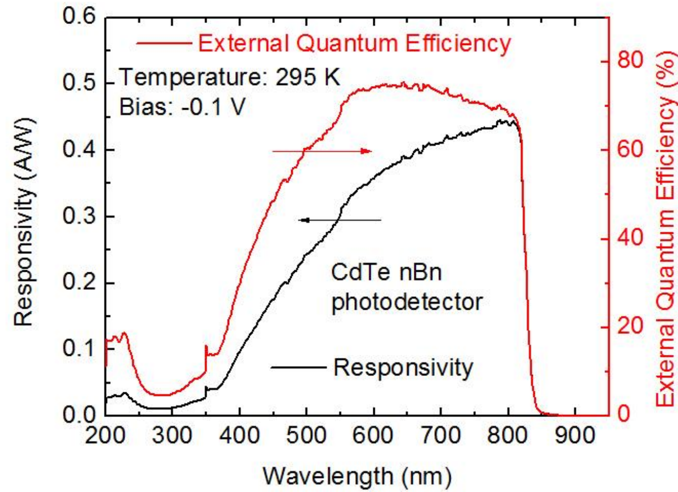

Figure 32 The spectral responsivity and external quantum efficiency of the CdTe nBn photodetector under an electrical bias of -0.1 V at room temperature.

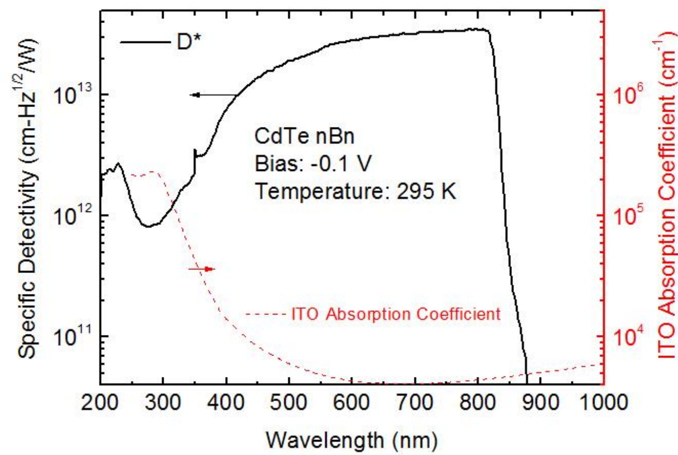

Figure 33 A high specific detectivity of up to 4×10^{13} cm-Hz$^{1/2}$/W at room temperature is achieved for the CdTe nBn photodetector. A flat detectivity plateau covers the whole visible light range

3.4 MWIR InSb PIN Photodetector

As the MWIR part of the CdTe/InSb two-color photodetector, InSb PIN photodetectors grown an n-type 5×10^{17} cm^{-3} InSb substrate have been fabricated and characterized. As in Figure 34, the photodetector consists of an undoped 1-µm-thick InSb absorber with an unintentional n-type doping concentration of ~10^{16} cm^{-3}, and a p-type 200-nm-thick top InSb layer with a doping concentration of 10^{19} cm^{-3} by Be. Mesas with a size of 400 × 400 µm^2 are defined by wet etch using citric acid solution (1 g citric acid: 1 mL water): H_2O_2 solution with a volume ratio of 50:1 after photolithography. The wet etch is stopped at the middle of the 500-nm-thick InSb buffer layer. Ti (20 nm) / Pt (20 nm) / Au (2000 nm) metal layers are deposited at the center of the mesa tops with a diameter of 200 µm, and are deposited at the backside of the substrate as the bottom contact.

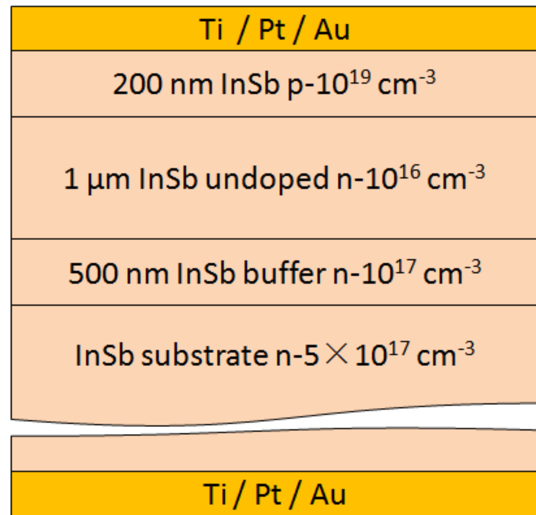

Figure 34 Layer structure of the InSb PIN photodetector

The InSb PIN photodetector shows a cut-off wavelength of 5.5 μm with a peak responsivity of 1.8 A/W at 4.5 μm, as in Figure 35. A plateau of external quantum efficiency over 50% covers the SWIR and MWIR regime from 1.5 μm to 4.5 μm, suggesting high material quality and effective collection of the photogenerated carriers by the Ohmic contacts.

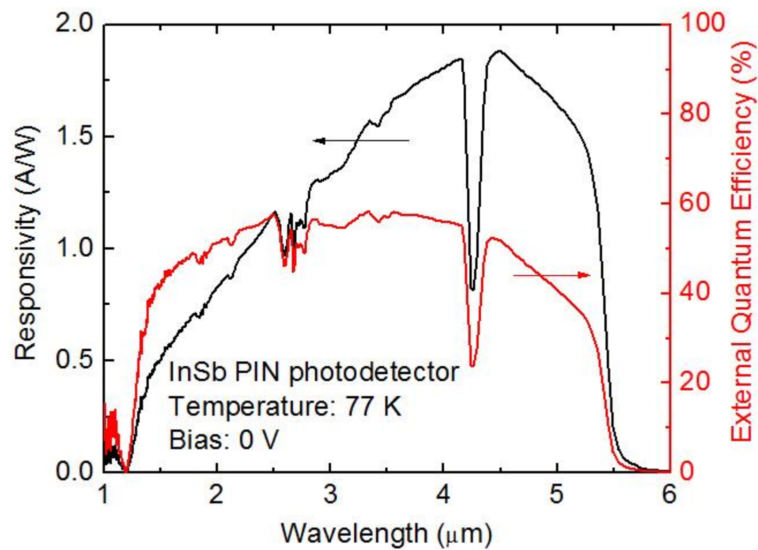

Figure 35 Spectral responsivity and eternal quantum efficiencies of the InSb PIN photodetector under 0 bias at 77 K

The dark I-V measurements show a high dark current of 0.5 A/cm^2 under -0.1 V bias and at 77 K, as in Figure 36. After submerging the sample in ammonium sulfide (20%): water solution with a volume ratio of 1: 1 for 30 min at room temperature, the dark current under -0.1 V is suppressed to 0.01 A/cm^2. The 0.01 A/cm^2 can be attributed to band-to-band tunneling current occurring in the unintentionally doped absorber layer

with an n-type doping concentration of ~ 10^{16} cm^{-3}. By reducing the n-type doping concentration of the InSb, it is possible to suppress the dark current further. It is reported that if the absorber layer of an InSb PN structure has an n-type doping concentration of ~ 10^{14} cm^{-3}, the dark current under -1 V at 77 K is below 10^{-6} A/cm^2 [60].

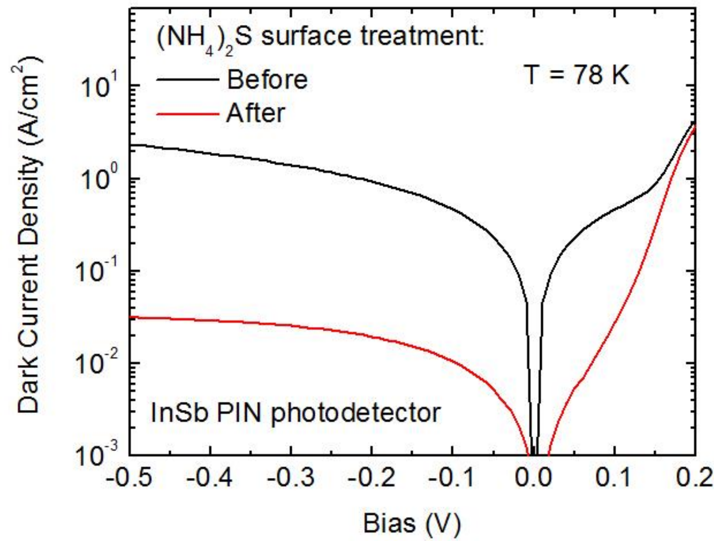

Figure 36 Dark I-V curves of the InSb PIN photodetector at 77 K before and after the ammounium-sulfide surface treatment

3.5 CdTe/InSb Visible/MWIR Two-Color Photodetector

After the demonstration of CdTe/InSb tunnel junctions, CdTe nBn photodetectors, and InSb PIN photodetectors, it becomes feasible to make a monolithically-integrated CdTe/InSb visible/MWIR two-color photodetector (2CPD). The design, growth, processing and characterization of such 2CPDs are discussed comprehensively in this chapter.

3.5.1 One Optical Bias

Only one external visible-light biasing source is required to optically address the CdTe/InSb 2CPDs because, in the dark, the CdTe sub-detector has a resistance much greater than that of the InSb sub-detector. This feature was reported in a near infrared and long-wave infrared 2CPD using GaAs PIN and GaAs/AlGaAs quantum well infrared sub-detectors [69]. Without any optical bias illumination, the CdTe/InSb 2CPD is dominated by the visible light response band, because the greater-resistance CdTe sub-detector limits the current through the device. To switch to the MWIR band, a visible optical bias with sufficient power is required to make the resistance of the CdTe sub-detector much smaller than that of the InSb sub-detector. However, the InSb sub-detector usually has a very small resistance due to its narrow bandgap, and the required optical bias power becomes impractically high. Undoped InSb grown using molecular beam epitaxy (MBE) usually has an unintentional n-type doping concentration higher than 10^{16} cm^{-3}, which gives a dark current higher than 10 A/cm^2 under -1 V at 77 K [60]. Therefore, an optical bias power of > 30 W/cm^2 is required to turn on the InSb sub-detector, which is so high that it damages the CdTe material. To minimize the required power of the optical bias, we use commercial undoped InSb substrates with unintentional n-type doping concentrations of ~ 10^{14} cm^{-3} as the absorber layer of the InSb PN structure, which ensures a dark current below 10^{-6} A/cm^2 under -1 V at 77 K [60]. Even though the InSb substrate is as thick as 500 μm, and has a low electron concentration of ~ 10^{14} cm^{-3}, the high electron mobility in the InSb (8×10^5 cm^{2}V^{-1}s^{-1}) ensures a negligible series resistance of 0.004 Ω-cm^2 induced by the InSb substrate.

Furthermore, an In/InSb Ohmic contact can be easily made on the back side of the undoped InSb substrate after proper annealing [70].

3.5.2 MBE Growth and Device Processing

Two CdTe/InSb 2CPD samples were grown on undoped, 2-inch InSb (100) substrates using a VG V80 solid-source MBE system. The layer structure in Figure 37(a) shows a CdTe-PN/InSb-PN structure (PN/PN for short) while Figure 37(b) shows a CdTe-nBn/InSb-PN structure (nBn/PN for short). For both of these structures, before the growth, the surface oxide of the InSb substrate is removed by heating the substrate to 480 °C for 60 min so that the defect density at the metallurgical junction of the InSb photodiode is minimized. The reflection high-energy electron diffraction (RHEED) shows a streaky 3×1 pattern when the oxide is removed. After the oxide removal, two 20-nm-thick p-type InSb layers with doping concentrations of 5×10^{17} cm^{-3} and 1×10^{19} cm^{-3} respectively, are grown in sequence. The samples are then transferred directly from the III-V chamber to a II-VI chamber in ultra-high vacuum. The II-VI material growth starts with a 20-nm-thick n-type CdTe contact layer with a doping concentration of 2×10^{18} cm^{-3}, which is followed by a 2.5-μm-thick undoped CdTe absorber layer. For the first sample with a CdTe PN structure, as in Figure 37(a), a 10-nm-thick $Mg_{0.3}Cd_{0.7}Te$ surface passivation layer is grown on top of the CdTe absorber layer, and a post-growth 8-nm-thick p-type amorphous silicon contact layer is deposited on the top, with a doping concentration of 1×10^{18} cm^{-3}. For the second sample with a CdTe nBn structure, as in Figure 37(b), a 300-nm-thick undoped CdZnTe alloy barrier layer with a graded Zn composition, from 0.5 to 1 is grown on top of the CdTe absorber to accommodate the

lattice mismatch between ZnTe and CdTe. Afterwards, a 50-nm-thick undoped ZnTe barrier layer and a 20-nm-thick undoped CdTe top contact layer are grown. Finally, circular 70-nm-thick ITO contacts with diameters of 0.5 mm are deposited on top of the two 2CPC samples, and a 200-nm-thick indium contact is deposited on the back side of the InSb substrates. The samples are annealed at 200 °C in air for 1 min to ensure an Ohmic indium/InSb contact. It is confirmed that the hetero p-InSb/n-CdTe interfaces in these 2CPDs have a low resistance of 0.04 Ω-cm^2 at 77 K by a stand-alone sample, which comprised of an n-type 10^{18} cm^{-3} CdTe layer grown on a p-type 10^{19} cm^{-3} InSb layer.

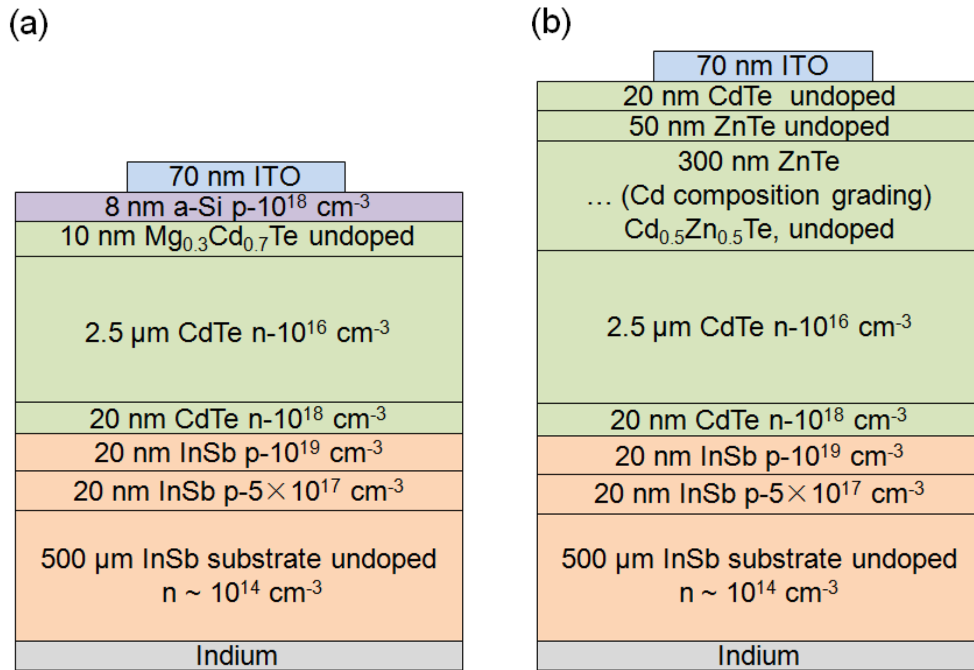

Figure 37 (a) Layer structure of the CdTe-PN/InSb-PN two-color photodetector. (b) Layer structure of the CdTe-nBn/InSb-PN two-color photodetector.

3.5.3 Electrical and Optical Addressing

The visible and MWIR responsivities as a function of the applied electrical and optical bias of both 2CPDs are plotted in Figure 38. The optical bias consists of a 532 nm CW laser with a power of 0.7 W/cm^2 with only two states, on or off, which means the optical bias is, or is not illuminating the devices. The visible and MWIR responsivities are represented by the responsivities at the wavelengths of 650 nm and 3.39 μm respectively. As in Figure 38, the responsivities are not only dependent on the optical bias states, but are also functions of the applied electrical bias. This is because both the optical and the electrical biases can change the quiescent points of the CdTe sub-detector and the InSb sub-detector, and then change the small-signal AC resistances of the two sub-detectors. The output of the 2CPD can be calculated by Equation (16) [71]:

$$i_{output} = \frac{r_{CdTe}}{r_{CdTe} + r_{InSb}} i_{visible} + \frac{r_{InSb}}{r_{CdTe} + r_{InSb}} i_{MWIR} \tag{16}$$

where $i_{visible}$ and i_{MWIR} are the AC photocurrents generated by the CdTe and InSb sub-detectors, r_{CdTe} and r_{InSb} are the small-signal AC resistances of the CdTe and InSb sub-detectors at the quiescent points respectively, and i_{output} is the AC output current signal of the 2CPD. According to Equation (16), the output photocurrent signal is dominated by the photocurrent of the CdTe sub-detector if $r_{CdTe} >> r_{InSb}$, whereas the photocurrent of the InSb sub-detector dominates if $r_{CdTe} << r_{InSb}$.

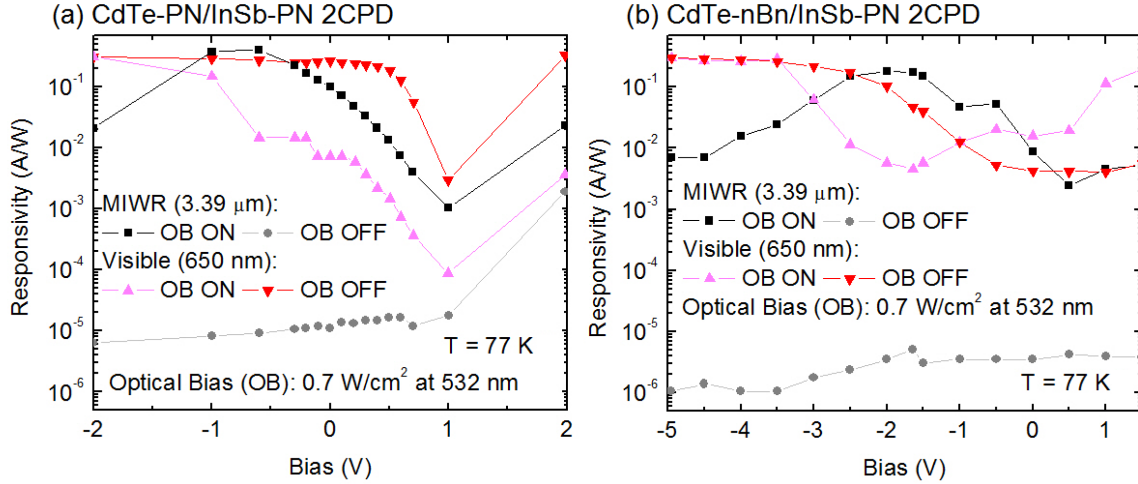

Figure 38 Responsivities of (a) the CdTe-PN/InSb-PN 2CPD and (b) the CdTe-nBn/InSb-PN 2CPD as a function of the applied electrical bias when the optical bias (OB) is ON or OFF at a temperature of 77 K. The MWIR and visible responsivities are measured using light sources at wavelengths of 3.39 µm and 650 nm respectively.

3.5.4 Band Switching

As in Figure 39, the devices are switched between the visible band (mode), with a 780 nm cut-off, and the MWIR band (mode), with a 5.5 µm cut-off, at 77 K under selected optical and electrical bias conditions, which are summarized in Table 4 (the visible-blind visible mode will be discussed later). For the PN/PN 2CPD, the band is switched by changing the optical bias only, while for the nBn/PN 2CPD, the band is switched by changing not only the optical bias, but also the electrical bias. In the visible mode, the two 2CPDs have a visible responsivity of up to ~ 0.3 A/W, covering the whole visible wavelength range, and a negligible MWIR responsivity of ~ 10^{-5} A/W. After switching to the MWIR mode, the MWIR responsivities are enhanced to 0.25 A/W and 0.75 A/W, and the visible responsivity is suppressed to 7.5 mA/W and 4.8 mA/W, for the

PN/PN 2CPD and the nBn/PN 2CPD respectively. The different absorption valleys in the MWIR spectra, as shown in Figure 39, can be attributed to the presence and absence of the lattice-mismatched CdZnTe and CdTe layers in the nBn/PN 2CPD and the PN/PN 2CPD, respectively.

Table 4 The electrical and optical bias conditions for different detecting modes of the two CdTe/InSb 2CPDs.

	Visible Mode	MWIR Mode
CdTe-PN/InSb-PN 2CPD	0 V, optical bias off	0 V, optical bias on
CdTe-nBn/InSb-PN 2CPD	-5 V, optical bias off	-1.64 V, optical bias on

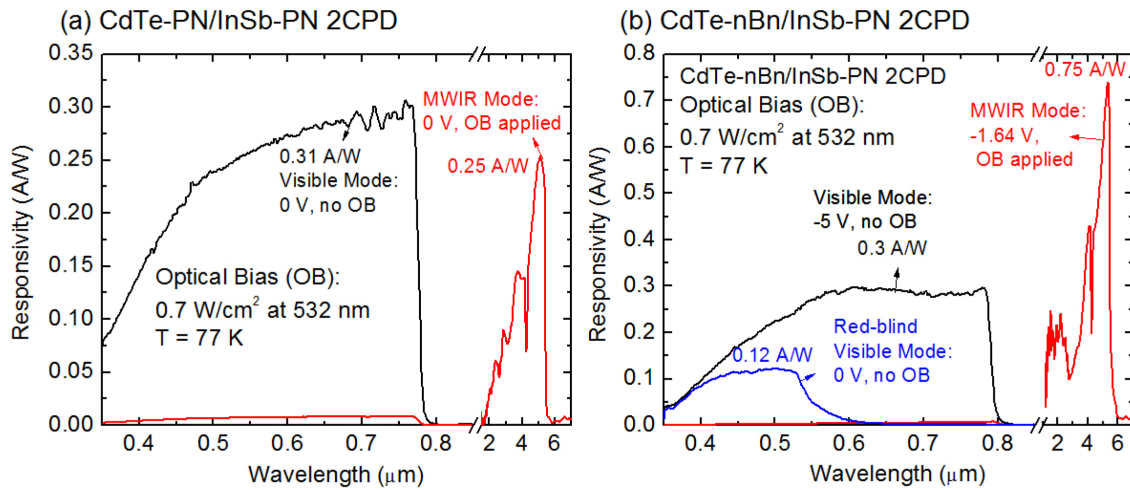

Figure 39 (a) The responsivity of the CdTe-PN/InSb-PN 2CPD can be switched between the visible band and the MWIR band by changing the optical bias only under a zero electrical bias. (b)The CdTe-nBn/InSb-PN 2CPD has responsivity bands of visible, MWIR and red-blind visible which are switchable by changing both the optical bias and the electrical bias.

The nBn/PN 2CPD has an extra band with a cutoff wavelength of ~ 550 nm and a responsivity of ~ 0.12 A/W (as in Figure 39(b)) under zero electrical bias, and with optical bias off, which is referred to as the red-blind visible mode. In this mode, the red-light responsivity is only 4.3 mA/W and the MWIR responsivity is as low as 3.5 μA/W. This feature is due to the absorption of the 350-nm-thick barrier layer and the particular band alignment of the CdTe nBn structure. Under zero electrical bias, and with the optical bias off, only the barrier layer is depleted by the built-in voltage. The photogenerated carriers in the barrier layer can be collected by the contacts whereas, most of the photogenerated carriers in the absorber layer recombine locally and contribute to a low red-light responsivity. As the applied electrical bias increases, under -5 V and with the optical bias off, both the barrier layer and the absorber layer are depleted, and the photogenerated carriers in both of these two layers can be collected efficiently, contributing to a responsivity covering the whole visible range, as in Figure 39(b). Similar phenomena have been reported in a Ga_2O_3/GaN Schottky-barrier photodetector [72], in which the Ga_2O_3 and GaN have nearly-aligned conduction band edges and a barrier in the valence band [73]. In addition, as in Figure 38(b), the feature can be now explained that, under an electrical bias from -1 V to 1.5 V, the 650-nm responsivity is enhanced significantly after turning on the optical bias. This is because the 532-nm optical bias reduces the barrier layer resistance significantly, and makes it more efficient at collecting photogenerated carriers from the absorber.

3.5.5 Device Specifications

Table 5 summarizes the specifications of the two devices including the peak responsivities, the BRRs, and the CTs for the visible and MWIR bands. To depict how much the responsivity is enhanced or suppressed, we use the band rejection ratio which is defined in Equation (17) [69].

$$BBR = 10\log\frac{R_{ON}}{R_{OFF}} \tag{17}$$

where log stands for denary logarithm, R_{ON} is the responsivity of a specific band when this band is switched on, and R_{OFF} is the responsivity of this band when it is switched off. On the other hand, to depict how much the undesirable MWIR (visible) photo response is when the devices are in the visible (MWIR) mode, we use visible to MWIR crosstalk (CT), and MWIR to visible CT which are defined as Equations (18) and (19), respectively [74].

$$CT_{MWIR}^{visible} = 10\log\frac{\int_0^\infty R_{MWIR}(\lambda)\,d\lambda}{\int_0^{1\mu m} R_{MWIR}(\lambda)\,d\lambda} \tag{18}$$

$$CT_{visible}^{MWIR} = 10\log\frac{\int_0^\infty R_{visible}(\lambda)\,d\lambda}{\int_{1\mu m}^\infty R_{visible}(\lambda)\,d\lambda} \tag{19}$$

where R is the responsivity, λ is the wavelength of the light, the subscript of the letters stands for which mode the device is in, and the superscript of the CTs stands for which band is undesirable. A higher CT value means lower undesirable photo response for each mode.

Table 5 The specifications of the CdTe-PN/InSb-PN and the CdTe-nBn/InSb-PN 2CPDs

	Peak $R_{visible}$ (A/W)	Peak R_{MWIR} (A/W)	Visible BRR (dB)	MWIR BRR (dB)	Visible to MWIR CT (dB)	MWIR to Visible CT (dB)
CdTe-PN /InSb-PN 2CPD	0.31	0.25	16	40	26	29
CdTe-nBn /InSb-PN 2CPD	0.30	0.75	18	52	31	40

By using both optical and electrical addressing, the nBn/PN 2CPD has achieved better specifications than the optically addressed PN/PN 2CPD, except for the peak visible responsivity. However, the MWIR responsivity of both of the two devices in the MWIR mode is still lower than the 1.8 A/W of a stand-alone InSb PIN photodetector, which is attributed to the free-carrier infrared absorption in the ITO contacts.

3.6 Chapter III Summary

Three building blocks to achieve a visible/MWIR CdTe/InSb two-color photodetector are studied, including a CdTe/InSb tunnel junction, a CdTe nBn photodetector and an InSb photodiode. n-CdTe/n-InSb and n-CdTe/p-InSb tunnel junctions have been demonstrated with very low resistances of 0.005 Ω-cm^2 and 0.04 Ω-cm^2, respectively at 80 K. A visible CdTe nBn photodetector with a cut-off wavelength of 820 nm has shown a specific detectivity of 3×10^{13} cm-Hz$^{1/2}$/W at room temperature. A 5.5-µm-cutoff epi-grown InSb PIN photodetector has been demonstrated a high dark current of 0.03 A/cm^2 at 77 K even after surface passivation. Such high dark current is attributed to a high unintentional doping concentration of 10^{16} cm^{-3} in the undoped

epi-grown InSb, and it can be suppressed significantly by using a commercial undoped InSb substrate with an unintentional doping concentration of $<10^{14}$ cm^{-3} as the absorber.

Furthermore, we have demonstrated two visible/MWIR two-color photodetectors (2CPD) grown on unintentionally doped InSb substrates using lattice-matched CdTe and InSb sub-detectors, which are monolithically integrated by an n-CdTe/p-InSb tunnel junction with a resistance of 0.04 Ω-cm^2 at 77 K. In these two 2CPDs, the CdTe sub-detector has a PN or nBn device structure, and the InSb sub-detector has a PN structure. By using selected optical bias and electrical bias conditions, the responsivity of these 2CPDs can be switched between a visible band with a cut-off of 870 nm and a MWIR band with a cut-off of 5.5 µm. The specifications of the optically-and-electrically addressed CdTe-nBn/InSb-PN 2CPD are generally superior compared to the optically addressed CdTe-PN/InSb-PN 2CPD. A MWIR responsivity of 0.75 A/W and a visible responsivity of 0.30 A/W, with band rejection ratios of 18 dB and 52 dB have been realized for the MWIR band and the visible band respectively.

The combination of electrical and optical addressing can be applied for future multicolor photodetectors based on other material systems. By changing the electrical bias, the required number of optical biases for addressing can be reduced compared to conventional pure optical addressing with many optical biases and under a constant electrical bias.

IV DEVICE PHYSICS OF NBN PHOTODETECTORS

4.1 Chapter IV Introduction

nBn photodetectors can be considered as an n-type photoconductor with a hetero-structure layer having a conduction band barrier to block the electrons, while a valance band edge aligned to the absorber layer to let the holes pass freely. In theory, it is plausible that if the n-type doping concentration is extremely high, the nBn photodetectors have extremely low dark current because the minority carriers have extremely low concentration and drift current. However, an nBn photodetector cannot be simply considered as a photoconductor with the drift current of the minority carriers only. Due to the band-to-band transitions, such as the thermal generation-recombination (G-R) process and band-to-band (BTB) tunneling process in the absorber, the dark current is actually enhanced if the n-type doping concentration is too high. The doping atoms can induce a lot of G-R trap centers and a high field that results in high BTB tunneling current.

Even though numerous experimental results have been reported to develop nBn photodetectors based on different materials [26][28][29][30][31][32], theoretical understanding of the device physics of nBn photodetectors was lacking until recently, however, now a range of numerical simulations and analytical modeling results have been reported [75][76][77][78][79]. Reine *et al.* [76] pointed out that an ideal nBn with identical doping concentration for the top contact layer and the absorber can be modeled by serially connected back-to-back double diodes. Under a negative voltage bias applied on the top contact, which can collect the photogenerated holes from the absorber layer, the top contact layer acts as a forwardly biased diode, and the absorber acts as a reversely

biased diode. In conventional pn junctions, people use the depletion approximation, and the boundary conditions of the minority carriers are as follows at the quasi-neutral-region/depletion-region interfaces.

$$p_n\left(V\right) = p_{n0}\exp(eV/kT) \tag{20}$$

$$n_p\left(V\right) = n_{p0}\exp(eV/kT) \tag{21}$$

Equations (20) and (21) stand if assuming the hole quasi Fermi level is flat in the depletion region and the p-type region, and the electron quasi Fermi level is flat in the depletion region and the n-type region. As shown in Figure 40, Reine *et al*. attributed the effectiveness of the back-to-back double diode model to the identical boundary conditions of the holes in the n-type layers of nBn, and in the n-type layers of the back-to-back double diodes [76]. This identicalness of the hole boundary conditions relies on the assumption that for the back-to-back double diodes, the hole quasi Fermi level is flat trough the depletion regions and the p-type layers, and for the nBn, the hole quasi Fermi level is flat through the barrier layer.

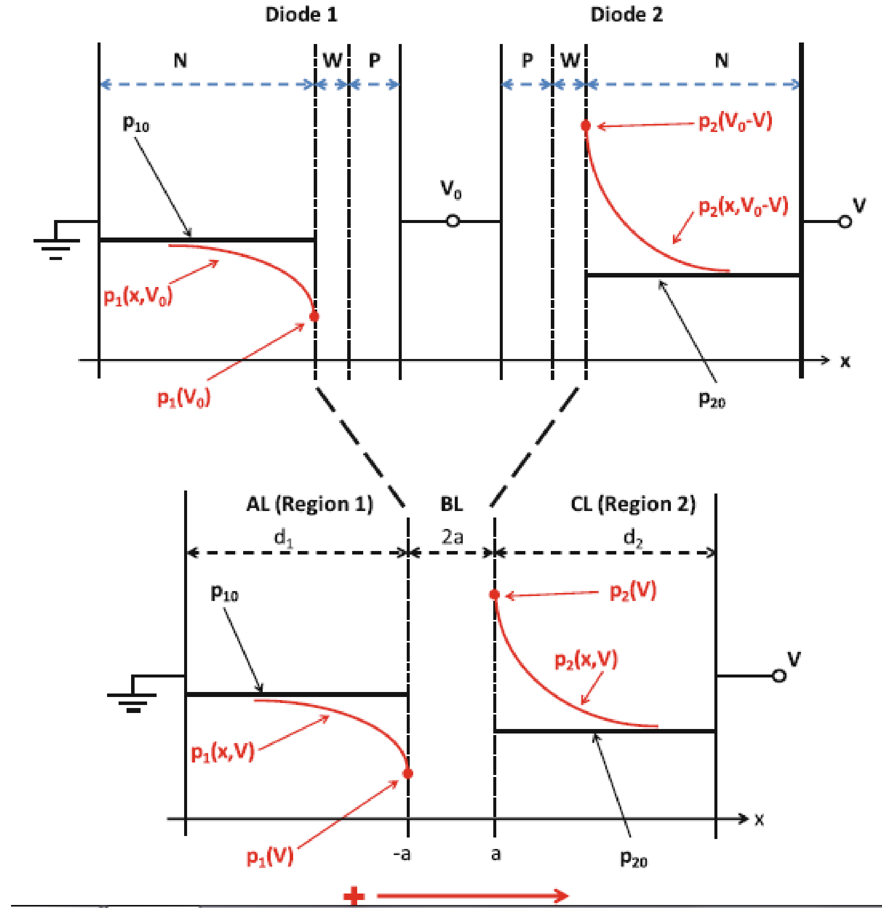

Figure 40 Equivalence of the boundary conditions on hole dark current in the back-to-back diode structure (above), and the nBn structure (below). The identical boundary conditions in both cases justify the use of the back-to-back photodiode equations to describe the nBn detector [76].

However, this back-to-back double diode model may be oversimplified under several circumstances. First, in practical nBn photodetectors, the top contact layer and the absorber layer may have different n-type doping concentrations, which is not the case as Reine et al. assumes. The absorber layer is unintentionally doped to ensure high material quality, whereas the top contact is heavily doped for Ohmic contact purposes. This

difference of doping concentrations gives rise to a built-in voltage that is not included in the back-to-back double diode model. Second, at high biases, due to the finite hole mobility of the barrier layer, the hole quasi Fermi level may tilt, as confirmed by simulations. This hole quasi Fermi level tilting in the nBn barrier layer may be different from that in the diode depletion regions, and therefore the hole boundary conditions becomes different under high bias and it undermines the effectiveness of the back-to-back diode model.

In this chapter, the device physics of nBn photodetector will be discussed from very fundamental aspects, such as the carrier generation, recombination, and transport in the nBn device. A novel concept of hole resistance is presented as possibly a more straightforward model than the back-to-back double diode model. In addition, analytical equations for dark current and the multicolor photodetection behavior of nBn photodetectors will be discussed.

4.2 Origin of the Dark Current

4.2.1 Carrier Generation, Recombination and Transport

The carrier transport and G-R process in the nBn structure are shown in the band edge diagram in Figure 41. For the sake of simplicity, the electron direct-tunneling current, the electron thermal emission current, the band-to-band tunneling current, and the surface leakage current are not considered. These currents are parallel to the dominant dark current to be discussed, and they can be simply added to the dominant dark current. In the top contact layer (TCL) on the left, the electrons are injected from the top metal contact, and accumulated due to the blocking of the barrier layer (BL). The holes are also

injected into the TCL by the field, **resulting in excess n and p deviating from the equilibrium concentrations**. Hence, the thermal recombination rate is larger than the thermal generation rate, and the net is thermal recombination in the TCL, which is referred to as net thermal recombination in the following text. In the absorber layer (AL), the electrons are collected by the bottom metal contact, and the holes in the AL are swept away by the high electrical field around the BL**, resulting in lower electron and hole concentrations than that of equilibrium concentrations**. Consequently, the thermal generation rate is higher than the recombination rate, and the net is thermal generation in the AL, which is referred to as net thermal generation in this essay.

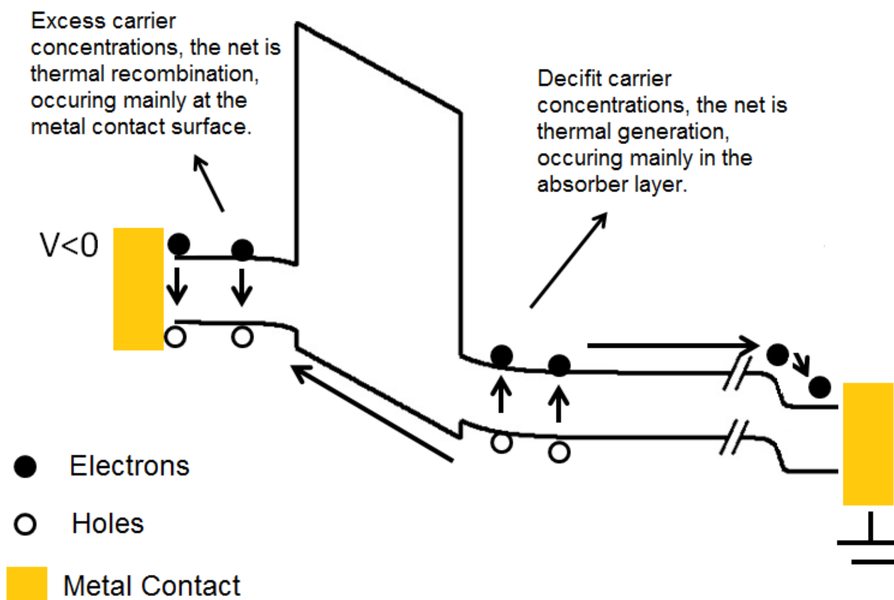

Figure 41 Carrier transport and G-R processes in the nBn structure

The carrier transport and G-R processes in the nBn structure can be further elucidated as follows. At steady state, we have the particle conservation equation for holes,

$$\nabla \cdot \overrightarrow{J_p} = q\left(G - R\right) \tag{22}$$

where J_p is the hole current density, G and R are the thermal generation and recombination rate in the T2SL respectively. Apply the Gauss theorem:

$$\oiint \overrightarrow{J_p} \cdot d\vec{s} = \iiint \nabla \cdot \overrightarrow{J_p} dV = q\iiint \left(G - R\right) dV \tag{23}$$

If the Gaussian surface of the AL is chosen, as in Figure 42, the hole current density in the BL, $I_{p,BL}$, equals the hole current density $I_{p,bc}$ at interface of the AL and bottom contact layer (BCL), plus the G-R process integration over the AL:

$$I_{p,BL} = I_{p,bc} + \frac{q\iiint_{AL}(G - R)dV}{A} \tag{24}$$

where A is the area of the nBn device. Similarly, if the Gaussian surface of the TCL is chosen as in Figure 42 (the left Gaussian surface is in the top metal contact), since the hole current in the metal contact is 0, the $I_{p,BL}$ equals the G-R process integration over the TCL and on the surface of the top metal contact:

$$I_{p,BL} = \frac{q\iiint_{TCL}(R - G)dV}{A} + \frac{q\iint_{contact}(R_S - G_S)dS}{A} \tag{25}$$

where R_S and G_S are the surface thermal recombination and generation rate respectively, at the top metal contact. In the BL, the electron current is almost 0, and there is negligible G-R in the BL, as a result the total dark current density equals the hole current density in the BL. If the hole diffusion length is assumed to be less than the AL thickness, the $I_{p,bc}$ term in Equation (24) is close to zero. So,

$$I = \frac{q\iiint_{TCL}(R-G)dV}{A} + \frac{q\iint_{contact}(R_S - G_S)dS}{A} \approx \frac{q\iiint_{AL}(G-R)dV}{A} \tag{26}$$

To summarize, Equation (26) means that the dark current of nBn structure, or the hole current flowing through the BL mainly originate from the net thermal generation in the AL, and they recombine with the electrons in the TCL and at the surface of the top metal contact.

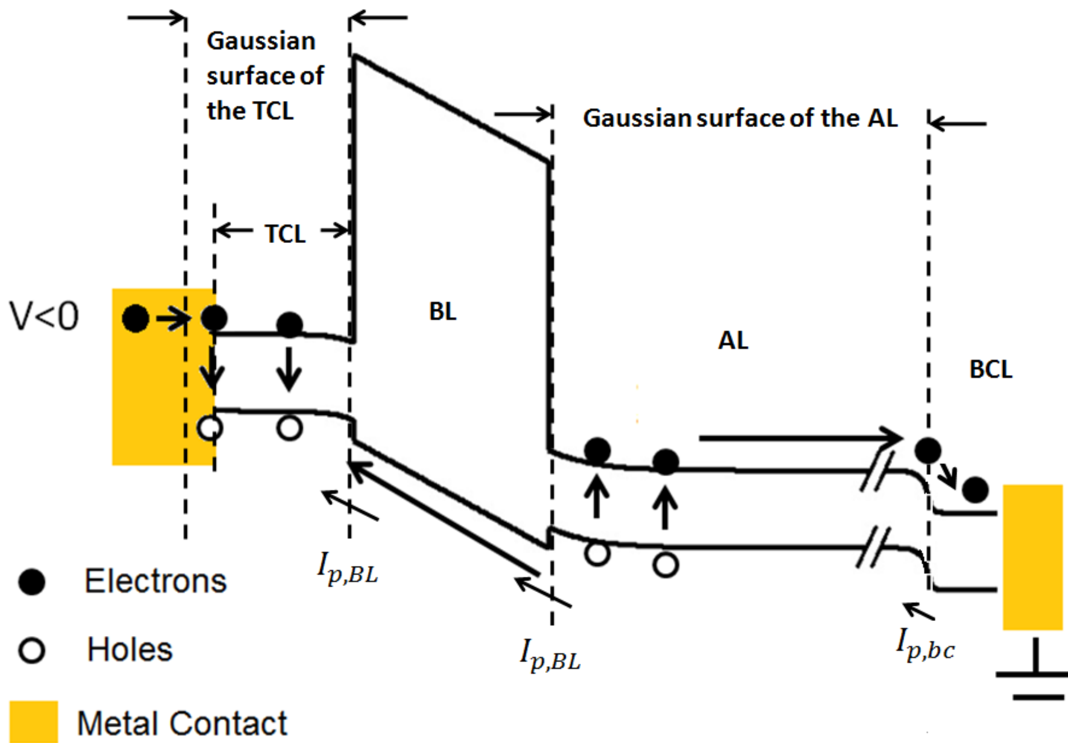

Figure 42 The Gauss theorem analysis of the hole current in the nBn structure.

4.2.2 Hole Impedance and Electrical Addressing

Because the AL and the TCL are connected in series, an important question is, which one, AL or the TCL is more resistive? The more resistive one should limit the total

current. In this chapter, the author proposes a novel way to depict how resistive the layers are in the nBn structure.

Generally speaking, the dark current is sufficiently determined by the profile of conduction/valence band edges, the profile of the electron quasi Fermi level (EQFL), and the profile of the hole quasi Fermi level (HQFL) for a given device. For the sake of simplicity to make the points clear, we consider the **near flat band condition** first: under small biases of 0 to -0.26 V near the V_{fb} of -0.13 V, the band bending in either the TCL or the AL is zero because of depletion or accumulation is negligible. As a useful fact, because the electrons are majority carriers and are blocked by the BL, the **EQFL is nearly flat in both the TCL and the AL**. As a consequence, **in the near flat band condition**, the current is only determined by the HQFL profile, which is determined by the two boundary conditions at the two ends, either in the TCL or the AL. In the TCL, the left end is the Ohmic contact, giving a boundary condition for the HQFL pinned to the equilibrium position at the contact surface. The other boundary condition is determined by how much the HQFL deviates from the equilibrium at the TCL/BL interface, which is referred to as $\Delta E_{fh,TCL}$, as in Figure 43(a). Once the boundary condition of $\Delta E_{fh,TCL}$ is given, the dark current in the TCL is determined. Similarly in the AL, because the diffusion length is assumed to be much less than the AL thickness, at the AL/BCL interface, the HQFL is very close to the equilibrium, and the dark current is only determined by how much the HQFL is separated from the equilibrium at the BL/AL interface, referred to as $\Delta E_{fh,AL}$, as in Figure 43(a). If the HQFL in the barrier is flat, which can be confirmed by Silvaco at low biases, $\Delta E_{fh,TCL}$ and $\Delta E_{fh,AL}$ are related to the applied voltage of V on the entire nBn, as in Figure 43(a):

$$V = \frac{\Delta E_{fh,TCL} + \Delta E_{fh,AL}}{q} \tag{27}$$

The current in the TCL and the AL should be identical because they are connected in series:

$$I_{TCL} = I_{AL} \tag{28}$$

where I_{TCL} and I_{AL} are functions of $\Delta E_{fh,TCL}$ and $\Delta E_{fh,AL}$, respectively. Now we have something very similar to voltage drop, but actually different from the voltage drop of the TCL and the AL: $\Delta E_{fh,TCL}$ and $\Delta E_{fh,AL}$. They are "applied" to the AL and the TCL layers, and generate some current. The "*hole impedance*" of the TCL and the AL can be then defined as Equations (29) and (30).

$$\Re_{h,TCL} = \frac{\Delta E_{fh,TCL}}{qI_{TCL}} \tag{29}$$

$$\Re_{h,AL} = \frac{\Delta E_{fh,AL}}{qI_{AL}} \tag{30}$$

Equation (27-30) show, an nBn structure can be interpreted as two hole impedances of the TCL and the AL connected in series. Once we know their I- ΔE_{fh} curves, the dark current of the nBn structure can be calculated at any bias, just as how the current is determined for two non-linear impedances connected in series.

Here, the author proposes a numerical method to calculate the I- ΔE_{fh} curves of the AL and the TCL in the **near flat band condition** using Silvaco. Take the calculation of the I- $\Delta E_{fh,AL}$ of the AL for example. In Silvaco, the I- $\Delta E_{fh,AL}$ of the AL can be calculated by setting the hole impedance of the TCL to be 0 artificially: simply set the hole mobility in the TCL and the BL to be extremely large (1×10^{12} cm^2/Vs), the minority

carrier lifetime in the TCL to be extremely short (1×10^{-6} ns), and leave all the other parameters as normal. We call this artificial nBn as nBn_AL. Figure 43(c) shows the simulation confirms the hole impedance of the TCL is 0 according to Equation (29), because the $\Delta E_{fh,TCL}$ is always 0 regardless of how much the applied bias and current are.

As Figure 43(c), in the nBn_AL, the total bias V equals $\Delta E_{fh,AL}/q$, and the dark current of the whole nBn_AL equals that of the AL, so we get the I- $\Delta E_{fh,AL}$ curve of the AL by calculating the I-V curve of the artificial nBn_AL. Admittedly, the band edges of the AL in the nBn_AL deviates slightly from that in the nBn, which would render a difference of the dark current, but in the **near flat band condition**, the difference can be negligible.

Similarly, as Figure 43(b), we can get the I- $\Delta E_{fh,TCL}$ curve of the TCL by setting artificially extreme material parameters for the BL and the AL, as in Table 6, and then calculating the I-V curve of the artificial nBn_TCL.

Table 6 The artificial material parameters of nBn_TCL, nBn_AL and nBn used in Silvaco

The minority carrier life time (ns)			
	Top contact layer	Barrier	Absorber
nBn_TCL	100		1×10^{-6}
nBn_AL	1×10^{-6}		100
nBn	100		100
The hole mobility ($cm^2V^{-1}s^{-1}$)			
	Top contact layer	Barrier	Absorber
nBn_TCL	5	1×10^{12}	1×10^{12}
nBn_AL	1×10^{12}	1×10^{12}	5
nBn	5	10	5

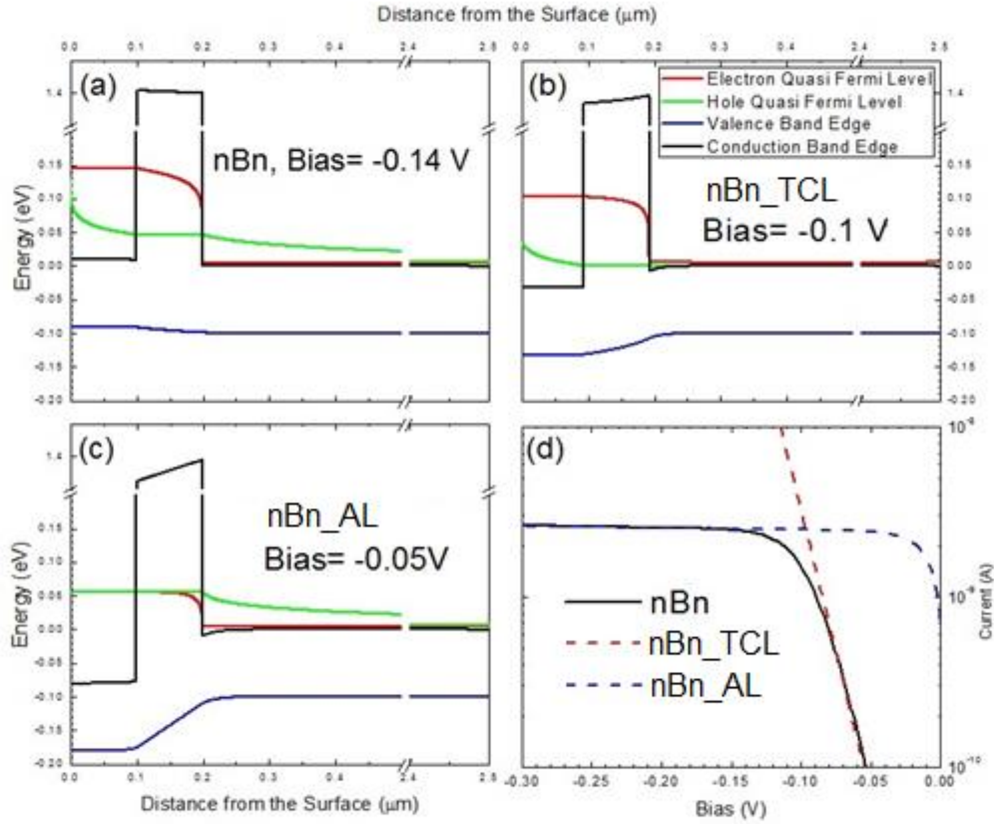

Figure 43 (a) The simulated four characteristic profiles: conduction and valence band edges, electron and hole quasi Fermi levels of the nBn at -0.14 V, (b) the four characteristic profiles of the artificial nBn_TCL at -0.1 V (c) the four characteristic profiles of the artificial nBn_AL at -0.05 V, (d) The dark I-V curves of the nBn, the nBn_TCL and the nBn_AL. (-0.1) + (-0.05) ≈ - 0.14 V! Temperature: 150K. The contacts are set to be Ohmic.

It is interesting to note that the band edges and quasi Fermi levels of the AL in Figure 43(a) imitates that in Figure 43(c), while the TCL in Figure 43(a) imitates that in Figure 43(b). Approximately, we have - 0.1 + (-0.05) ≈ - 0.14 V, which confirms Equation (27). Furthermore, the I-V curves of nBn, nBn_AL, and nBn_TCL in Figure

43(d) show that, for any other given current, the sum of the voltages of the nBn_AL and the nBn_TCL always equals the voltage of the nBn. In other words, Equation (27) stands always.

The numerical simulation shows that, an nBn structure can be considered as two non-linear **hole impedances** of the AL and the TCL connected in series. The I-ΔE_{fh} curves of the AL and the TCL are shown in Figure 43(d). The exponentially increasing I-V curve of nBn_TCL, in Figure 43(d), suggests that the TCL in the nBn behaves like a forwardly biased PN junction. While the saturated I-V curve of nBn_AL indicates that the AL in the nBn is like a reversely biased PN junction. At a low bias regime (0 ~ -0.13 V), *the TCL* has higher hole impedance and it limits the dark current as a forward PN junction, while at a higher bias regime (-0.13 V ~ -0.5 V), the AL has higher hole impedance and it limits the dark current as a reverse PN junction.

In summary, the hole impedance model clearly shows that the dark current of nBn photodetectors has an electrical-addressing behavior. If a negative electrical bias is applied on the top contact, the dark current is dictated by the thermal, or Shockley-Read-Hall (SRH) net generation process in the CdTe absorber. In contrast, if a positive electrical bias is applied on the top contact, the dark current is dictated by the SRH net generation process in the top CdTe layer. At high voltage biases, the hole quasi Fermi level tilts in the barrier layer, and the sum of $\Delta E_{fh,TCL}$ and $\Delta E_{fh,AL}$ as in Equation (29) and (33) is less than the applied total voltage. Therefore, at high voltage biases, the dark current of nBn is in theory lower than the dark current calculated by using the dark I-V curves of the artificial nBn_TCL and nBn_AL photodetectors as in Figure 43(b).

4.3 Two-color Photodetection

The photocurrent of an nBn photodetector has a similar electrical-addressing behavior as the dark current, because photo-generated carriers have to go through the identical process as Figure 41, except the generation step is realized by photo-excitation rather than thermal excitation as the dark current. Consequently, if a negative (positive) bias is applied on the top, the photocurrent signal exclusively originates from the photon absorption in the absorber (top contact layer). This characteristic can be utilized to make an electrically-addressed two-color photodetector by making the TCL in the nBn structure optically thick, and have a bandgap greater than the AL, but still smaller than the BL. A bias-selectable dual-band mid-/long-wavelength nBn infrared photodetector has been reported based on InAs/InAsSb type-II superlattices [80].

Furthermore, an alternative way to make a two-color photodetector based on an nBn structure is to make the BL optically thick, while keeping the TCL much thinner than optical penetration depth. As discussed in Chapter 3.5.4, an extra red-blind visible band of the CdTe nBn photodetector is due to the absorption of the 300-nm-thick Zn(Cd)Te barrier layer. Similarly, Weng et al. reported a β-Ga_2O_3/GaN Schottky-Barrier Photodetector which has a responsivity spectrum dependent on the applied voltage [72]. The Ga_2O_3 is 200 nm thick on the GaN with an aligned conduction band edge and a large valence band offset [73].

4.4 Analytical Equations

At operating (negative) bias when the AL limits the current, the BL can be considered as a capacitor with two-dimensional electron gas (2DEG) in the TCL, and a

uniform positive space charge region distributed in the AL. If using the depletion approximation, positive charge with a density of N_D is distributed uniformly in the depletion region with the width of $W_{dep.}$ The BL has fully ionized doping atoms and a uniform positive charge density of N_D. Therefore, in the electron accumulation layer of the TCL the negative sheet charge density is $N_D(t_b + W_{dep})$ to meet the charge neutrality principle. The total potential drop across the entire device equals the total applied voltage V minus V_{fb}, namely the sum of the potential drops in the TCL, in the BL, and in the AL:

$$\varphi = V - V_{fb} = \varphi_{TCL} + \varphi_{AL} + \varphi_{BL} \tag{31}$$

where V_{fb} is the flat band voltage. It equals the change of Fermi level at equilibrium induced by the different doping concentration in the TCL and the AL.

The TCL is heavily doped and the potential drop due to the 2DEG in the accumulation layer is negligible:

$$\varphi_{TCL} \approx 0 \tag{32}$$

The potential drop in the absorber layer can be calculated by solving the Poisson's equation:

$$\varphi_{AL} = \frac{qN_D W_{dep}^2}{2\varepsilon_s} \tag{33}$$

where ε_S is the static dielectric constant of the InAs/InAsSb T2SL.

The barrier layer is un-intentionally doped, so:

$$\varphi_{BL} = \frac{qN_D W_{dep}}{C_{BL}} + \frac{qN_{D,\mathrm{BL}} t_{BL}}{2C_{BL}} \tag{34}$$

where C_{BL} equals to ε_{BL}/t_{BL}, which is the capacitance per unit area of the barrier layer, ε_{B} is the dielectric constant of the barrier layer, ε_{BL} is the thickness of the barrier layer, N_D and $N_{D,BL}$ are the donor concentration in the AL and the BL respectively.

Remarkably, the highest allowed bias to avoid depletion of the absorber layer can be calculated using Equation (35), by combining Equations (31-34) and letting $W_{dep} = 0$.

$$V_{\max} = V_{fb} + \frac{qN_{D,BL}t_{BL}}{2C_{BL}} \tag{35}$$

The width of the depletion region W_{dep} of the absorber layer under a voltage V greater than V_{max} can be calculated as Equation (36) by combining Equations (31-34).

$$W_{dep} = \frac{\varepsilon_s}{C_{BL}}\left(\sqrt{1+\frac{2C_{BL}^2\left|V-V_{\max}\right|}{q\varepsilon_s N_D}}-1\right) \tag{36}$$

The total current of nBn photodetectors can be then analytically expressed as [25]:

$$I_{dark} \approx I_{G-R} + I_{diffusion} \approx \frac{qn_iW_{dep}}{\tau_{SRH}} + \frac{qL_pn_i^2}{\tau_pN_D} \tag{37}$$

where n_i is the intrinsic carrier concentration of the T2SL, N_D is the unintentionally doped density in the AL, τ_{SRH} is the Shockley-Read-Hall carrier lifetime in the depletion region of the AL, V_{fb} is the flat-band voltage, q is the elementary charge, L_P is the vertical hole diffusion length in the absorber and τ_P is the hole carrier lifetime in the quasi-neutral region of the absorber. It is important to note that in Equation (37), the first term is the G-R current originating from the depletion region, and the second term is the diffusion current originating from the quasi-neutral region in the AL. All the other currents are parallel to this current and can be simply added to Equation (37), such as the electron

direct-tunneling current, the electron thermal emission current, the band-to-band tunneling current, and the surface leakage current.

4.5 Chapter IV Summary

The device physics of nBn structure with a perfect valence-band edge alignment is comprehensively discussed. The origin of the dark current is elucidated from a fundamental aspect by analyzing the carrier generation, recombination and transport in the nBn structure. Furthermore, a physical model of hole impedance is presented as a more straightforward model than the back-to-back double diode model to understand the device physics of nBn photodetectors.

Remarkably, a typical characteristic of nBn photodetector, electrical addressing, is well explained after this careful analysis of the device physics of the nBn structure. By applying a voltage bias with different polarities, the dark current is limited by the net thermal generation, or the photocurrent is dominantly contributed by the light absorption in different layers of the nBn photodetector. By making the top contact layer and the absorber layer optically thick, and the former with a greater band gap than the latter, it is possible to have an electrically-addressed two-color photodetector.

In addition, analytical equations are presented to estimate the depletion width of the absorber layer, highest bias allowed to avoid depletion of the absorber layer, and the dark current of nBn photodetectors.

V CONCLUSIONS

This work develops the concept of nBn photodetectors by demonstrating a mid-wave infrared (MWIR) InAs/InAsSb superlattice nBn photodetector with charge output and a visible CdTe nBn photodetector with current output. Furthermore, the CdTe nBn photodetector is integrated monolithically with an InSb photodiode to achieve a visible/MWIR two-color photodetector (2CPD). In addition, the device physics of nBn photodetectors with aligned valence band edges is elucidated comprehensively.

The MWIR nBn photodetector has an absorber layer and a barrier layer with type-II band edge alignment, so that a potential well is present in the barrier layer as confirmed by electron holography measurements. Under light illumination at temperatures below 77 K, photogenerated holes are collected and stored in this well under low biases < -0.2 V, which induce low dark current of $<10^{-5}$ A/cm^2. A lifetime of up to 40 s for the stored holes is confirmed by photocurrent and photo-capacitance decay measurements. The number of the photo-charge stored in the well is an integration of the photocurrent over time, and therefore the photo-charge signal has a noise much lower than the photocurrent signal. Also, the photo-charge can be collected by the well at near-zero voltage, which ensures low dark current and dark noise. Since the charges can be read out laterally along the barrier layer as in charge-coupled devices (CCD), it is possible to make nBn photodetectors with charge output which have much improved noise figures than the conventional nBn photodetectors with current output.

The visible nBn photodetector with conventional current output is achieved by using high-quality CdTe as the absorber layer, and ZnTe as the barrier layer. These two

materials as a nearly perfect valence band alignment with an offset of only -0.05 eV. By using an novel ITO/undoped-CdTe top contact design, the 820-nm-cutoff CdTe nBn photodetector has reached a peak specific detectivity (D*) of 3×10^{13} cm-Hz$^{1/2}$/W at room temperature under -0.1 V. This high-quality CdTe nBn photodetector is further integrated with a 5.5-μm-cutoff InSb photodiode monolithically to achieve a visible/MWIR 2CPD. The nBn structure of the CdTe sub-detector makes it necessary to use both electrical optical biases to switch the photo response of the 2CPD between the two colors. At 77 K, the photo responsivity can be switched between a visible band with peak responsivity of ~ 0.3 A/W, and a MWIR band with peak responsivity of ~ 0.75 A/W. The band rejection ratio is 18 dB for the visible band, 52 dB for the MWIR band. This monolithically integrated visible/MWIR 2CPD enables future focal plane arrays with high fill-factor and the capability of switching between visible and MWIR colors.

In addition, the device physics of nBn photodetectors with aligned valence band edge isclarified comprehensively. After careful analysis of carrier generation-recombination and transport processes, a "hole impedance" model is presented to explain the origin of the dark current and the electrically-addressed two-color photodetection characteristics. This model is more straightforward than the conventional back-to-back double diode model and can be used for future nBn photodetectors based on different materials.

REFERENCES

[1] A. Rogalski, K. Chrzanowski, *Metrol. Meas. Syst.* **XXI(4)**, 565 (2014).

[2] A. Rogalski, *Prog. Quant. Electron.* **27**, 59 (2003).

[3] A. Rogalski, *Rep. Prog. Phys.* **68**, 2267 (2005).

[4] V. C. Lopes, A. J. Syllaios, and M. C. Chen, *Semicond. Sci. Technol.* **8**, 824 (1993).

[5] P. Manurkar, S. Ramezani-Darvish, B.-M. Nguyen, M. Razeghi, and J. Hubbs, *Appl. Phys. Lett.* **97**, 193505 (2010).

[6] E. R. Youngdale, J. R. Meyer, C. A. Hoffman, F. J. Bartoli, C. H. Grein, P. M. Young, H. Ehrenreich, R. H. Miles, and D. H. Chow, *Appl. Phys. Lett.* **64**, 3160 (1994).

[7] C. H. Grein, P. M. Young, M. E. Flatte, and H. Ehrenheich, *J. Appl. Phys.* **78**, 7143 (1995).

[8] J. R. Meyer, C. L. Felix, W. W. Bewley, I. Vurgaftman, E. H. Aifer, L. J.Olafsen, J. R. Lindle, C. A. Hoffman, M.-J. Yang, B. R. Bennett, B. V. Shanabrook, H. Lee, C.-H. Lin, S. S. Pei, and R. H. Miles, *Appl. Phys. Lett.* **73**, 2857 (1998).

[9] B. C. Connelly, G. D. Metcalfe, H. Shen, and M. Wraback, *Appl. Phys. Lett.* **97**, 251117 (2010).

[10] D. Donetsky, G. Belenky, S. Svensson, and S. Suchalkin, *Appl. Phys. Lett.* **97**, 052108 (2010).

[11] E. H. Steenbergen, B. C. Connelly, G. D. Metcalfe, H. Shen, M. Wraback, D. Lubyshev, Y. Qiu, J. M. Fastenau, A. W. K. Liu, S. Elhamri, O. O. Cellek, and Y.-H. Zhang, *Appl. Phys. Lett.* **99**, 251110 (2011).

[12] Z.-Y. Lin, S. Liu, E. H. Steenbergen, and Y.-H. Zhang, *Appl. Phys. Lett.* **107**, 201107 (2015).

[13] P. T. Webster, N. A. Riordan, S. Liu, E. H. Steenbergen, R. A. Synowicki, Y.-H. Zhang, and S. R. Johnson, *Appl. Phys. Lett.* **106**, 061907 (2015).

[14] D. Zuo, R. Liu, D. Wasserman, J. Mabon, Z.-Y. He, S. Liu, Y.-H. Zhang, E. A. Kadlec, B. V. Olson, and E. A. Shaner, *Appl. Phys. Lett.* **106**, 071107 (2015).

[15] Y.-H. Zhang, *Appl. Phys. Lett.* **66**, 118 (1995).

[16] http://asumbe.eas.asu.edu

[17] P. Norton, *Opto-electron. Rev.* **10(3)**, 159 (2002).

[18] A. Rogalski, J. Antoszewski, and L. Faraone, *J. Appl. Phys.* **105**, 091101 (2009).

[19] F. H. L. Koppens, T. Mueller, Ph. Avouris, A. C. Ferrari, M. S. Vitiello, and M. Polini, *Nat. Nanotechnol.* **9**, 780 (2014).

[20] http://meroli.web.cern.ch/meroli/lecture_cmos_vs_ccd_pixel_sensor.html

[21] Jun Ohta, *Smart CMOS Image Sensors and Appliactions*, (2007).

[22] M. Bigas, E. Cabruja, J. Forest, and J. Salvi, *Microelectron. J.* **37**, 433 (2006).

[23] Y. Kang, H.-D. Liu, M. Morse, M. J. Paniccia, M. Zadka, S. Litski, G. Sarid, A. Pauchard, Y.-H. Kuo, H.-W. Chen, W. S. Zaoui, J. E. Bowers, A. Beling, D. C. McIntosh, X. Zheng and J. C. Campbell, *Nat. Photon.* **3**, 59 (2009).

[24] P. C. Klipstein, U. S. Patent 7,795,640, (2003).

[25] S. Maimon and G. W. Wicks, *Appl. Phys. Lett.* **89**, 151109 (2006).

[26] P. C. Klipstein, Proc. of SPIE Infrared Technology and Applications XXXIV, 69402U (2008).

[27] S. Mou, J. V. Li, and S. L. Chuang, *J. Appl. Phys*. **102**, 066103 (2007).

[28] A. Soibel, C. J. Hill, S. A. Keo, L. Hoglund, R. Rosenberg, R. Kowalczyk, A. Khoshakhlagh, A. Fisher, D Z.-Y. Ting, and S. D. Gunapala, *Appl. Phys. Lett.* **105**, 023512 (2014).

[29] A. M. Itsuno, J. D. Phillips, and S. Velicu, *Appl. Phys. Lett.* **100**, 161102 (2012).

[30] J. B. Rodriguez, E. Plis, G. Bishop, Y. D. Sharma, H. Kim, L. R. Dawson, and S. Krishna, *Appl. Phys. Lett.* **91**, 043514 (2007).

[31] H. S. Kim, O. O. Cellek, Z.-Y. Lin, Z.-Y. He, H. Li, S. Liu, and Y.-H. Zhang, *Appl. Phys. Lett.* **101**, 161114 (2012).

[32] A. Haddadi , G. Chen , R. Chevallier , A. M. Hoang , and M. Razeghi, *Appl. Phys. Lett.* **105**, 121104 (2014).

[33] W. H. Rolls, *Electro-Opt. Syst. Des.* **9**(11), 10 (1977).

[34] J. C. Campbell, T. P. Lee, A. G. Dentai, and C. A. Burrus, *Appl. Phys. Lett.* **34**, 401 (1979).

[35] M. J. Sun, W. S. C. Chang, and C. M. Wolfe, *Appl. Opt.* **17**, 3533 (1978).

[36] E. F. Schulte, U.S. Patent No. 5,113,076 (12 May 1992).

[37] E. P. G. Smith, L. T. Pham, G. M. Venzor, E. M. Norton, M. D. Newton, P. M. Goetz, V. K. Randall, A. M. Gallagher, G. K. Pierce, E. A. Patten, R. A. Coussa, K. Kosai, W. A. Radford, L. M. Giegerich, J. M. Edwards, S. M. Johnson, S. T. Baur, J. A. Roth, B. Nosho, T. J. De Lyon, J. E. Jensen, R. E. Longshore, *J. of Elect. Mater.* **33**, 509-516 (2004).

[38] A. Haddadi, R. Chevallier, G. Chen, A. M. Hoang, and M. Razeghi, *Appl. Phys. Lett.* **106**, 011104 (2015).

[39] Y.-H. Zhang, D. Ding, E. Steenbergen, U.S. Patent No. 8,350,208 B1 (8 Jan 2013).

[40] E. H. Steenbergen, M. J. DiNezza, W. H. G. Dettlaff, S. H. Lim, Y.-H. Zhang, *Appl. Phys. Lett.* **97** 161111 (2010).

[41] E. F. Schulte, U. S. patent 5113076 A (1992).

[42] O. O. Cellek, Z.-Y. He, Z.-Y. Lin, H. S. Kim, S. Liu and Y.-H. Zhang, Proceedings of SPIE Vol. 8631, 86311I (2013).

[43] X.-M. Shen, Z.-Y. He, S. Liu, Z.-Y. Lin, Y.-H. Zhang, D. J. Smith, and M. R. McCartney, *Appl. Phys. Lett.* **107**, 122109 (2015).

[44] J. D. Vincent, *Fundamentals of Infrared Detector Operation and Testing*, Page 139 (1989).

[45] E. Burstein, *Phys, Rev.* **93**, 632 (1954).

[46] T. S. Moss, *Proc. Phys. Soc.* **B76**, 775 (1954).

[47] Y.-F. Lao, P. K. D. D. P. Pitigala, A. G. U. Perera, E. Plis, S. S. Krishna, and P. S. Wijewarnasuriya, *Appl. Phys. Lett.* **103**, 181110 (2013).

[48] K. Ploog, G.H. Döhler, *Adv. Phys.* **32**, 285 (1983).

[49] Y.-H. Zhang, N. N. Ledentsov, and K. Ploog, *Phys. Rev.* **B44**, 1399 (1991).

[50] W. S. Boyle and G. E. Smith, *Bell Syst. Tech. J.* **49**, 587 (1970).

[51] K. Banerjee, S. Ghosh, S. Mallick, E. Plis, S. Krishna, and C. Grein, *Appl. Phys. Lett.* **94**, 201107 (2009).

[52] http://investor.firstsolar.com/releasedetail.cfm?releaseid=956479

[53] S. Del Sordo, L. Abbene, E. Caroli, A. M. Mancini, A. Zappettini, and P. Ubertini, *Sensors* **9**, 3491 (2009).

[54] M. J. DiNezza, X.-H. Zhao, S. Liu, A. P. Kirk and Y.-H. Zhang, *Appl. Phys. Lett.* **103**, 193901 (2013).

[55] X.-H. Zhao, M. J. DiNezza, S. Liu, C. M. Campbell, Y. Zhao and Y.-H. Zhang, *Appl. Phys. Lett.* **105**, 252101 (2014).

[56] S. Liu, X.-H. Zhao, C. M. Campbell, M. B. Lassise, Y. Zhao and Y.-H. Zhang, *Appl. Phys. Lett.* **107**, 041120 (2015).

[57] Y. Zhao, M. Boccard, S. Liu, J. Becker, X.-H. Zhao, C. M. Campbell, E. Suarez, M. B. Lassise, Z. Holman, and Y.-H. Zhang, *Nat. Energy* **1**, 16067 (2016).

[58] J.-H. Yang, W.-J. Yin, J.-S. Park, J. Burst, W. K. Metzger, T. Gessert, T. Barnes and S.-H. Wei, *J. Appl. Phys.* **118**, 025102 (2015).

[59] Z.-Y. He, C. M. Campbell, M. B. Lassise, Z.-Y. Lin, J. J. Becker, Y. Zhao, M. Boccard, Z. Holman, and Y.-H. Zhang, *Appl. Phys. Lett.* **109**, 121112 (2016).

[60] J. Abautret, A. Evirgen, J.P. Perez, P. Christol, A. Rouvié, R. Cluzel, A. Cordat, J. Rothman, Proc. of SPIE 8993 899314-1 (2014).

[61] D. Rioux, D. W. Niles, and H. Höchst, *J. Appl. Phys*. **73**, 8381 (1993).

[62] B. Späth, J. Fritsche, A. Klein, and W. Jaegermann, *Appl. Phys. Lett.* **90**, 062112 (2007).

[63] X.-H. Zhao, S. Liu, Y. Zhao, C. M. Campbell, M. B. Lassise, Y.-S. Kuo, and Y.-H. Zhang, IEEE J. Photovoltaics, vol. 6, no. 2, pp. 552-556, (2016).

[64] C.-H. Su, *J. Appl. Phys.* **103**, 084903 (2008).

[65] X.-H. Zhao, C. M. Campbell, M. B. Lassise, and Y.-H. Zhang, unpublished results.

[66] http://www.eotech.com/content/userfiles/12.5GHz%20Photodetectors.pdf

[67] These specs are for commercial devices, such as the products shown on this website. http://assets.newport.com/webDocuments-EN/images/Detection_Systems.PDF

[68] These specs are for commercial devices, such as the products shown on this website. https://www.thorlabs.us/newgrouppage9.cfm?objectgroup_id=285

[69] O. O. Cellek, J. L. Reno, Y.-H. Zhang, *Appl. Phys. Lett.* **100**, 241103 (2012).

[70] S. Hishiki, I. Kanno, O. Sugiura, R. Xiang, T. Nakamura, and M. Katagiri, *IEEE T NUCL SCI* 52, NO. 6 (2005).

[71] O. O. Cellek and Y.-H. Zhang, Proc. SPIE 8268, 8268N (2012).

[72] W. Y. Weng, T. J. Hsueh, S. J. Chang, G. J. Huang, and H. T. Hsueh, *IEEE PHOTONIC TECH L* 23, NO. 7 (2011).

[73] W. Wei, Z. Qin, S. Fan, Z. Li, Ka. Shi, Q. Zhu and G. Zhang, *Nanoscale Res. Lett.* **7**, 562(2012).

[74] A. Nedelcu, X. Marcadet, O. Huet, and P. Bois, *Appl. Phys. Lett.* **88**, 191113 (2006).

[75] Schuster, C.A. Keasler, M. Reine, and E. Bellotti, *J. Electron. Mater.* **41**, 2981 (2012).

[76] M. Reine, J. Schuster, B. Pinkie, and E. Bellotti, *J. Electron. Mater.* **42**, 3015 (2013).

[77] M. Reine, B. Pinkie, J. Schuster, and E. Bellotti, *J. Electron. Mater.* **43**, 2915 (2014).

[78] P. Martyniuk, W. Gawron, and A. Rogalski, *J. Electron. Mater.* **42**, 3309 (2013).

[79] P. Martyniuk and A. Rogalski, *Opt. Eng.* **53**, 017106 (2014).

[80] A. Haddadi, R. Chevallier, G. Chen, A. M. Hoang, and M. Razeghi, *Appl. Phys. Lett.* **106**, 011104 (2015).